

Stokes and the Brinkmanlets

Harry Wiffen

Collingwood College

Advised by Dr. Adam Townsend

A DISSERTATION PRESENTED FOR THE DEGREE OF
Master of Mathematics



Department of Mathematical Sciences
Durham University
United Kingdom

May 2025

Declaration

This piece of work is a result of my own work and I have complied with the Department's guidance on multiple submission and on the use of AI tools. Material from the work of others not involved in the project has been acknowledged, quotations and paraphrases suitably indicated, and all uses of AI tools have been declared.

Contents

Declaration	ii
1 Introduction	1
2 The falling Stokeslets	5
2.1 The Stokes equations	5
2.2 Deriving a Stokeslet	7
2.3 Forming a particle cloud	12
2.4 Simulating the cloud	14
2.5 Analysing particle spread	18
3 The Brinkmanlets	21
3.1 Darcy's law	21
3.2 The Brinkman equations	22
3.3 Solving the Brinkman equations	23
3.4 Deriving a Brinkmanlet	27
3.5 Deriving a regularised Brinkmanlet	29
4 The falling Brinkmanlets	36
4.1 Forming a particle cloud II	36
4.2 High permeability simulations	37
4.3 Decreasing the permeability	38
4.4 Analysing particle spread II	40
5 Further model complexities	43
5.1 Magnetised particle flow	43
5.2 An alternative particle geometry	48
6 Conclusion	51
Bibliography	54

Chapter 1

Introduction

Stokes flows describe the fluid motion in systems where the viscous forces significantly outweigh the inherent inertia of the fluid. Such flows are governed by the Stokes equations—a low Reynolds number approximation of the Navier–Stokes equations. Stokes flows are critical to a multitude of scientific disciplines, particularly when studying fluids on microscopic length scales or under extremely slow-moving conditions. Such applications range from modelling blood flow in capillaries, to analysing the sedimentation of particles in quiescent fluids.

The hydrodynamic problem of modelling a falling cloud of particles in a highly viscous fluid is one which has been extensively covered. In 1997, Nitsche and Batchelor [27] introduced an analytical methodology which exploits the linearity of the Stokes equations, using the principle of superposition, to model a particle cloud. They modelled each particle as an infinitesimal point-force, using the fundamental solution of the Stokes equations—commonly referred to as a Stokeslet. Their subsequent analysis consisted of the numerical simulation of these clouds, as they sedimented under gravity, with up to 320 particles. They found that the clouds maintained their initial structure as they fell, with a vertical trail of particles slowly lost from the top.

However, alternative studies using a larger number of particles, such as the works of Adachi, Kiriyama and Yoshioka in 1978 [1] and Machu et al. in 2001 [24], attained a different conclusion. They observed the particle cloud begin to take the form of a torus, which subsequently split into a number of smaller clusters. An illustration of the evolution of such a cloud, from the work of Machu et al. [24] can be seen in fig. 1.1.

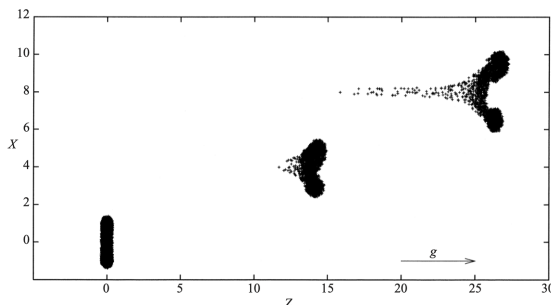


Figure 1.1: Temporal evolution of a particle cloud, from the work of Machu et al. in [24]. Rotated for visual compactness.

The work of Metzger, Nicolas and Guazzelli in 2007 [25], which provides the foundation of the analysis in chapter 2, develops the methodology introduced by Nitsche and Batchelor [27] in order to perform a more comprehensive analysis of the cloud behaviour. Using the Stokeslet approximation, with up to 3 000 particles, they simulated the cloud sedimentation and observed the aforementioned torus formation and splitting phenomena. Furthermore, they performed an experimental analysis, which supported the numerical observations and hence validated the point-particle approach.

In chapter 2, we derive the analytical framework behind the Stokeslet model, before analysing the behaviour of a falling cloud, using a modern implementation of Runge–Kutta numerical integration. We then evaluate the impact of the initial particle density within the cloud on its evolution. Further complexities to the falling cloud model have been introduced, such as in the work of Ma and Pan in 2024 [23]. They modelled the lubrication and multi-body effects—which are neglected by the point-particle model—using a complex neural network of interacting particles. Such developments are beyond the scope of this paper.

In 2001, Cortez [7] proposed an evolution to the Stokeslet model, in which the force through each particle is concentrated through a ‘blob function’, which acts as a regularised approximation to the Dirac delta measure. This approach removes the singularity of the Stokeslet and leads to a smoothing effect of the flow in the immediate vicinity of each particle. In 2005, Cortez, Fauci and Medovikov [8] extended this approach to the three-dimensional Stokes equations, using the resulting regularised Stokeslet solution in the modelling of helical swimmers. A visual demonstrating the evolution of these swimmers, from the work of Cortez, Fauci and Medovikov [8], can be seen in fig. 1.2.

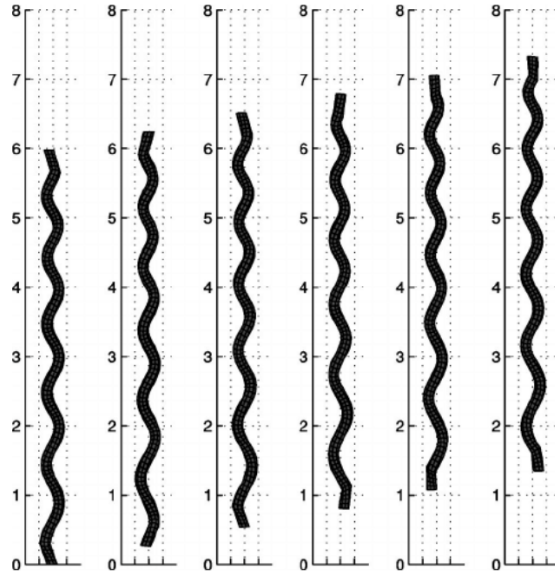


Figure 1.2: Dynamic evolution of a helical swimmer, submersed in a highly viscous fluid, from the work of Cortez, Fauci and Medovikov in [8]. The helical body is discretised using 100 rings—with 8 points per ring—with internal motors at each end of the body.

Another important application of Stokes flows is in the approximate modelling of fluids through a porous medium. In such environments, due to the small spacing between solid inclusions in the medium, fluids are typically very slow-moving. However, it has

been shown that the universality of this model does not extend to all porous media. Qualitative differences in the fluid behaviour arise as the permeability of the medium changes. The Brinkman equations address these inaccuracies, by interpolating between the Stokes equations and Darcy's law—which describes a pressure-driven fluid flow. Brinkman flows are hence commonly used in a number of fields, from hydrogeology to coffee brewing. The latter of these applications was discussed by Giacomini et al. in 2020 [17], where the flow of hot water through a porous medium of coffee grains was modelled as a Brinkman flow. A schematic visualisation of this porous medium, from the work of Giacomini et al. [17], can be seen in fig. 1.3.

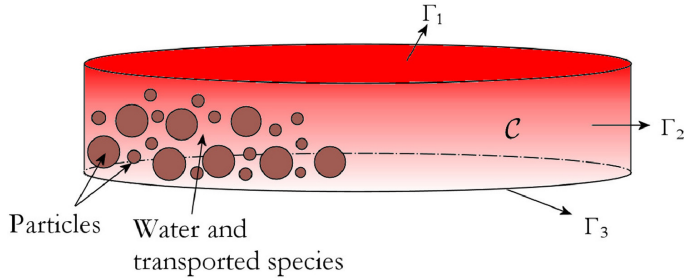


Figure 1.3: Schematic diagram of the geometry of an espresso pod, modelled as a cylindrical Brinkman medium, by Giacomini et al. in [17]. The faces of the cylindrical domain are given by Γ_i for $i \in \{1, 2, 3\}$.

In 2010, Cortez et al. [9] obtained the fundamental solution to the Brinkman equations—known as a Brinkmanlet. They then developed a regularised Brinkmanlet, using an adaptation of the blob function approach. In chapter 3, we introduce Darcy's law and motivate the derivation of the Brinkman equations. We then expand upon the methodology outlined in [9], in order to rigorously obtain both fundamental and regularised Brinkmanlets.

In chapter 4, we propose and implement a modification to the point-particle model, wherein we superpose Brinkmanlets in order to model a falling cloud in a Brinkman fluid. This allows us to analyse the impact of porous media, with varying degrees of permeability, on the behaviour of the cloud. We successfully simulate Brinkman flows through a multitude of theoretical mediums, resulting in qualitatively different dynamics. By assessing the behaviour through a medium with perfect permeability, we validate the asymptotic alignment of the Brinkman equations with the Stokes equations. Finally, we analyse the impact of different media on the rate of particle dispersion. Due to applications of the Brinkman equations in certain hydrodynamic research, such as the modelling of groundwater flows [11], such inferences provide valuable insights into the varying effects of porous media.

Many practical applications of Stokes flows and Brinkman flows involve complex external forces and intricate particle geometries. For example, in 2010, Hatzikonstantinou and Vafeas [20] described how many fluid flows of physical interest occur in the presence of a magnetic field. The ability to incorporate additional forces which arise from these fields into numerical simulations is therefore of great theoretical interest.

In chapter 5, we generalise our existing computational framework, allowing us to model any complex construction of external forces. We then illustrate this development using a conceptual model of hydromagnetic particle flow. A further analysis of particle dispersion in this enhanced model then demonstrates the impact of such fields on Brinkman flows.

In 2001, Machu et al. [24] analysed the sensitivity of the initial particle arrangement on the subsequent evolution of the cloud, during sedimentation. Similarly, in a recent 2025 article,

Daddi-Moussa-Ider and Vilfan [10] discussed Brinkman flows in a multitude of complex geometries, with a wide range of biological applications. One result by Daddi-Moussa-Ider and Vilfan [10], where Brinkman flows were evaluated around point forces placed in the centre of vertical pipes, can be seen in fig. 1.4. These studies exemplify the importance of flexibility in numerical simulations, with respect to initial particle geometries.

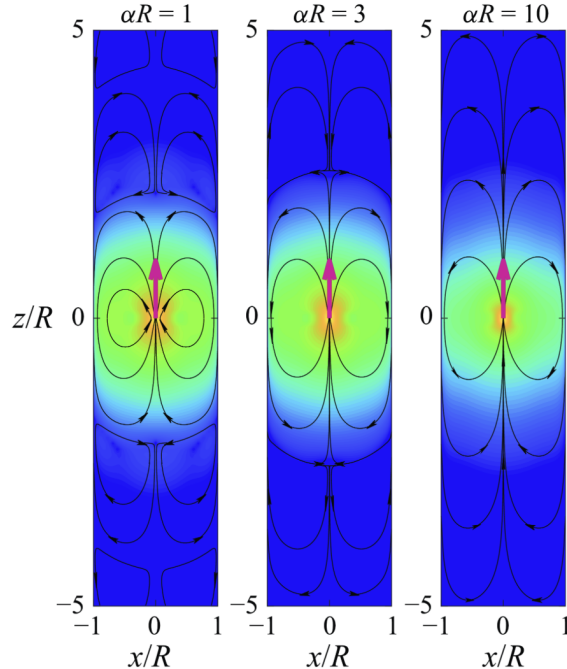


Figure 1.4: Brinkman flow streamlines around point forces, placed in the centre of vertical pipes—taken from the work of Daddi-Moussa-Ider and Vilfan in [10]. R is the radius of the pipe and α is a characteristic permeability parameter of the Brinkman medium. The colour gradient represents the non-dimensional magnitude of the flow velocity.

Using the advanced computational framework established in chapter 5, we are able to simulate the evolution of any initial particle configuration—with any external forces. We demonstrate this using a simplified model of a three-dimensional articulated body, consisting of regularised Brinkmanlets, attached by elastic springs.

This paper provides a comprehensive coverage of Stokes flows, particularly with respect to the popular and widely applicable point-force model. We then adapt this model to the context of fluid flows through porous media, via the Brinkman equations, providing insights into the effects of medium permeability. Using a more advanced and generalised numerical framework, we demonstrate the impact of additional model complexities on simulation outcomes. Whilst these models are purely conceptual, they demonstrate the versatility of our computational set-up—exemplifying how it could be used for future research, across an array of scientific disciplines.

Note that all code used in the creation of this paper can be found in the corresponding [GitHub repository](#) [30]. The code is written in [Python](#) and [R](#) and the repository also includes online, interactive simulation results written in [HTML](#). For more information, see the associated [README](#) file.

Chapter 2

The falling Stokeslets

In this chapter, we derive the Stokes equations by introducing the concept of the Reynolds number, before solving for the fundamental solution—the Stokeslet. We then construct a particle cloud, using the point-force model presented by Nitsche and Batchelor in 1997 [27]. Finally, we computationally simulate the particle cloud as it settles under gravity, for a variety of initial conditions.

2.1 The Stokes equations

We begin with a set of equations which underpins much of Newtonian fluid mechanics—the incompressible Navier–Stokes equations. These are

$$\begin{aligned} \rho \frac{\partial \mathbf{u}}{\partial t} + \rho(\mathbf{u} \cdot \nabla) \mathbf{u} &= \mu \nabla^2 \mathbf{u} - \nabla p + \mathbf{F}, \\ \nabla \cdot \mathbf{u} &= 0, \end{aligned} \tag{2.1.1}$$

where ρ is the fluid density, \mathbf{u} is the fluid velocity, μ is a dynamic viscosity, p is a pressure field and \mathbf{F} is a vector of external forces [29].

The first of these equations, fundamentally, represents the conservation of momentum [16]. The left-hand side contains the inertial terms of the fluid, whilst the right-hand side is made up of the forces which instigate this acceleration. Respectively, these are the friction generated by the fluid viscosity, the forces arising from the pressure gradient, and any external forces acting on the fluid body. The second equation represents the conservation of mass, and is simple due to the incompressibility assumption [29].

In order to mathematically distinguish between qualitatively different fluid flows, we introduce a concept known as the Reynolds number. As explained by Trombley and Ekiel-Jeżewska in [29], this is a positive, dimensionless property which characterises, broadly, the dynamics that a fluid will exhibit. It is defined as

$$Re = \frac{\rho U L}{\mu}, \tag{2.1.2}$$

where U and L are characteristic velocity and length scales of the fluid, respectively. It encapsulates a number of properties intrinsic to each flow, and its use becomes clear when considering the differing behaviour between high ($Re \gg 1$) and low ($Re \ll 1$) Reynolds number flows.

We can accurately approximate the dynamics of different flows by considering the asymptotic behaviour of the Navier–Stokes equations at each Reynolds number limit. A large Reynolds number implies that the viscosity, relative to the inertial forces, is negligible. Physically, this results in rapid, turbulent flow. Mathematically, it can be shown that, upon taking $Re \rightarrow \infty$, this behaviour is reflected within the Navier–Stokes equations, with the viscosity forces vanishing [26].

Stokes flows occur within fluids which are highly viscous, and thus have negligible inertial terms. Consequently, such flows are represented by a low Reynolds number—so we will examine the behaviour of these flows by considering the Navier–Stokes equations in the limit $Re \rightarrow 0$. Of course, as the Reynolds number is a dimensionless property made up of characteristic scales, in order to calculate this limit, we must first non-dimensionalise the Navier–Stokes equations. As in [29], we introduce the substitutions

$$\mathbf{u} = U\hat{\mathbf{u}}; \quad \nabla = \frac{1}{L}\widehat{\nabla}; \quad \frac{\partial}{\partial t} = \frac{U}{L}\frac{\partial}{\partial \hat{t}}; \quad p = \frac{\mu U}{L}\hat{p}; \quad \mathbf{F} = \frac{\mu U}{L^2}\widehat{\mathbf{F}},$$

where the hats represent dimensionless values. Using these scales, the Navier–Stokes equations (2.1.1) become

$$\begin{aligned} \frac{U^2}{L}\frac{\partial \hat{\mathbf{u}}}{\partial \hat{t}} + \frac{U^2}{L}(\hat{\mathbf{u}} \cdot \widehat{\nabla})\hat{\mathbf{u}} &= \frac{\mu U}{\rho L^2}\widehat{\nabla}^2\hat{\mathbf{u}} - \frac{\mu U}{\rho L^2}\widehat{\nabla}\hat{p} + \frac{\mu U}{\rho L^2}\widehat{\mathbf{F}}, \\ \widehat{\nabla} \cdot \hat{\mathbf{u}} &= 0, \end{aligned}$$

and multiplying through by $\rho L^2/\mu U$, we get

$$\begin{aligned} \frac{\rho U L}{\mu}\frac{\partial \hat{\mathbf{u}}}{\partial \hat{t}} + \frac{\rho U L}{\mu}(\hat{\mathbf{u}} \cdot \widehat{\nabla})\hat{\mathbf{u}} &= \widehat{\nabla}^2\hat{\mathbf{u}} - \widehat{\nabla}\hat{p} + \widehat{\mathbf{F}}, \\ \widehat{\nabla} \cdot \hat{\mathbf{u}} &= 0. \end{aligned}$$

Now, we note that on the left-hand side of the first equation, the common cofactor is precisely the value which we previously defined to be the Reynolds number, in eq. (2.1.2). Thus, taking this to zero, the non-dimensional Navier–Stokes equations reduce to

$$\begin{aligned} \widehat{\nabla}^2\hat{\mathbf{u}} - \widehat{\nabla}\hat{p} + \widehat{\mathbf{F}} &= \mathbf{0}, \\ \widehat{\nabla} \cdot \hat{\mathbf{u}} &= 0. \end{aligned}$$

As the system has now been simplified, we can re-dimensionalise the variables in order to allow calculations with precise physical parameters. This gives us

$$\begin{aligned} \frac{L^2}{U}\nabla^2\mathbf{u} - \frac{L^2}{\mu U}\nabla p + \frac{L^2}{\mu U}\mathbf{F} &= 0, \\ \nabla \cdot \mathbf{u} &= 0, \end{aligned}$$

which, finally, simplifies to give us the Stokes equations for an incompressible fluid

$$\begin{aligned} \mu\nabla^2\mathbf{u} - \nabla p &= -\mathbf{F}, \\ \nabla \cdot \mathbf{u} &= 0. \end{aligned} \tag{2.1.3}$$

It is clear that the low Reynolds number assumption has resulted in a significant simplification of the Navier–Stokes equations. Not only have we eliminated any time dependency

from the system, we have also removed any terms which exhibit non-linear behaviour. Hence, due to the principle of superposition, it holds that any linear combination of solutions is itself a solution [29].

To show this, consider a pair of solutions, say $(\mathbf{u}_1(\mathbf{r}), p_1(\mathbf{r}))$ and $(\mathbf{u}_2(\mathbf{r}), p_2(\mathbf{r}))$, arising from external forces \mathbf{F}_1 and \mathbf{F}_2 , respectively. Then, consider the linear combinations

$$\mathbf{u} = \alpha \mathbf{u}_1 + \beta \mathbf{u}_2; \quad p = \alpha p_1 + \beta p_2; \quad \mathbf{F} = \alpha \mathbf{F}_1 + \beta \mathbf{F}_2,$$

for some $\alpha, \beta \in \mathbb{R}$. For this new velocity and pressure, the left-hand side of the Stokes momentum equation (2.1.3) can be written as

$$\mu \nabla^2 \mathbf{u} - \nabla p = \mu \nabla^2 (\alpha \mathbf{u}_1 + \beta \mathbf{u}_2) - \nabla (\alpha p_1 + \beta p_2),$$

which, due to the linearity of the operators, can be rearranged to give

$$\begin{aligned} \mu \nabla^2 \mathbf{u} - \nabla p &= \alpha (\mu \nabla^2 \mathbf{u}_1 - \nabla p_1) + \beta (\mu \nabla^2 \mathbf{u}_2 - \nabla p_2), \\ &= -\alpha \mathbf{F}_1 - \beta \mathbf{F}_2, \\ &= -\mathbf{F}. \end{aligned}$$

That is, $(\mathbf{u}(\mathbf{r}), p(\mathbf{r}))$ satisfies the Stokes momentum equation for the combined force, \mathbf{F} . The incompressibility property can similarly be shown to hold, by expressing the divergence of \mathbf{u} as

$$\begin{aligned} \nabla \cdot \mathbf{u} &= \nabla \cdot (\alpha \mathbf{u}_1 + \beta \mathbf{u}_2), \\ &= \alpha (\nabla \cdot \mathbf{u}_1) + \beta (\nabla \cdot \mathbf{u}_2), \\ &= 0, \end{aligned}$$

where the final line arises as a result of the incompressibility of \mathbf{u}_1 and \mathbf{u}_2 . Thus, we have shown that $(\mathbf{u}(\mathbf{r}), p(\mathbf{r}))$ is a solution to the Stokes equations (2.1.3), for the external force $\mathbf{F} = \alpha \mathbf{F}_1 + \beta \mathbf{F}_2$.

This is an extremely useful property which means that, if a fluid body is subject to multiple external forces, we can solve for the superposed resulting flow by simply combining the individual solutions arising from each external force. This property will play a crucial role in our simulations, but we first need to obtain the fundamental solution of the Stokes equations.

2.2 Deriving a Stokeslet

This method was first proposed by Zapryanov and Tabakova in [31] and we build upon the general framework outlined by Lisicki in [22], to provide a detailed derivation of the fundamental solution of a Stokes system.

We consider the scenario in which a point particle, placed at the origin and suspended in a viscous fluid body, experiences a force, \mathbf{F} . Our objective is to determine the resultant flow at some position \mathbf{r} —relative to the point particle—which arises from the force. This fundamental set-up can be seen in fig. 2.1.

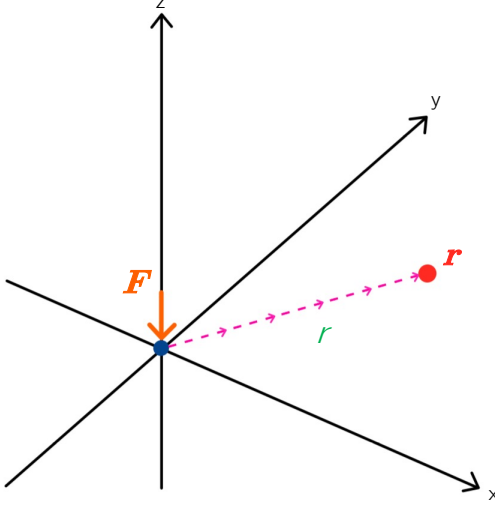


Figure 2.1: Visualisation of the fundamental Stokes set-up. The flow at point \mathbf{r} , which is a distance of $|\mathbf{r}| = r$ from the origin, arises as a result of a force, \mathbf{F} .

In this regime, the Stokes equations (2.1.3) have the form

$$\begin{aligned} \mu \nabla^2 \mathbf{u} - \nabla p &= -\mathbf{F} \delta(\mathbf{r}), \\ \nabla \cdot \mathbf{u} &= 0, \end{aligned} \quad (2.2.1)$$

where $\delta(\cdot)$ is the Dirac delta measure, representing the concentration of the force through the point. We impose the boundary conditions of $\mathbf{u}, p \rightarrow 0$ as $|\mathbf{r}| = r \rightarrow \infty$, representing how the effect of the point-force becomes negligible as we move arbitrarily far away.

Throughout this derivation, we make frequent use of Fourier transforms. As such, we begin by establishing, for some function f , the Fourier transform pair

$$\begin{aligned} \mathcal{F}[f] &= \widehat{f}(\mathbf{k}) := \int_{\mathbb{R}^3} f(\mathbf{r}) e^{-i\mathbf{k}\cdot\mathbf{r}} d\mathbf{r}, \\ \mathcal{F}^{-1}[f] &= f(\mathbf{r}) := \frac{1}{(2\pi)^3} \int_{\mathbb{R}^3} \widehat{f}(\mathbf{k}) e^{i\mathbf{k}\cdot\mathbf{r}} d\mathbf{k}. \end{aligned}$$

Next, we derive a number of useful properties from the fundamental solutions of the Laplace and biharmonic equations. Namely, these are functions ϕ and ψ which respectively satisfy

$$\nabla^2 \phi(\mathbf{r}) = -\delta(\mathbf{r}), \quad (2.2.2)$$

$$\nabla^4 \psi(\mathbf{r}) = -\delta(\mathbf{r}). \quad (2.2.3)$$

In 3D, these solutions are well-known [22], and have the form

$$\phi(\mathbf{r}) = \frac{1}{4\pi r}; \quad \psi(\mathbf{r}) = \frac{r}{8\pi},$$

where $r = |\mathbf{r}|$. By expressing the Dirac delta measure directly as an inverse Fourier transform, eq. (2.2.2) can be written as

$$\nabla^2 \left(\frac{1}{4\pi r} \right) = -\delta(\mathbf{r}) = \frac{-1}{(2\pi)^3} \int_{\mathbb{R}^3} \widehat{\delta}(\mathbf{k}) e^{i\mathbf{k}\cdot\mathbf{r}} d\mathbf{k},$$

where $\hat{\delta}(\mathbf{k})$, by our Fourier transform definition, is

$$\begin{aligned}\hat{\delta}(\mathbf{k}) &= \int_{\mathbb{R}^3} \delta(\mathbf{r}) e^{-i\mathbf{k}\cdot\mathbf{r}} d\mathbf{r}, \\ &= e^{-i\mathbf{k}\cdot\mathbf{0}}, \\ &= 1,\end{aligned}$$

with the second line arising from the definition of the Dirac delta within an integral. Next, we note that one may write $\nabla^2 \left(\frac{1}{4\pi r} \right) = \nabla \cdot \nabla \left(\frac{1}{4\pi r} \right)$ and hence, by the derivative property of a Fourier transform, we have

$$\nabla \left(\frac{1}{4\pi r} \right) = \frac{1}{i\mathbf{k}} \nabla^2 \left(\frac{1}{4\pi r} \right).$$

Thus, using the Laplacian form above, then multiplying through by $i\mathbf{k}/i\mathbf{k}$, we obtain our first key result

$$\begin{aligned}\nabla \left(\frac{1}{4\pi r} \right) &= \frac{-1}{i\mathbf{k}(2\pi)^3} \int_{\mathbb{R}^3} e^{i\mathbf{k}\cdot\mathbf{r}} d\mathbf{k}, \\ &= \frac{i}{(2\pi)^3} \int_{\mathbb{R}^3} \frac{\mathbf{k}}{k^2} e^{i\mathbf{k}\cdot\mathbf{r}} d\mathbf{k},\end{aligned}\tag{2.2.4}$$

where $k = |\mathbf{k}|$. By the same logic, the derivative property also gives us our next result

$$\begin{aligned}\frac{1}{4\pi r} &= \frac{1}{i\mathbf{k}} \nabla \left(\frac{1}{4\pi r} \right), \\ &= \frac{1}{(2\pi)^3} \int_{\mathbb{R}^3} \frac{1}{k^2} e^{i\mathbf{k}\cdot\mathbf{r}} d\mathbf{k}.\end{aligned}\tag{2.2.5}$$

Repeating this process for the biharmonic equation (2.2.3), we initially determine that

$$\nabla^4 \left(\frac{r}{8\pi} \right) = \frac{-1}{(2\pi)^3} \int_{\mathbb{R}^3} e^{i\mathbf{k}\cdot\mathbf{r}} d\mathbf{k},$$

then, once again applying the derivative property, we deduce that

$$\nabla \left(\frac{r}{8\pi} \right) = \frac{-1}{(2\pi)^3} \int_{\mathbb{R}^3} \frac{i\mathbf{k}}{k^4} e^{i\mathbf{k}\cdot\mathbf{r}} d\mathbf{k}.$$

Finally, we now consider the tensor product

$$\nabla \otimes \nabla \left(\frac{r}{8\pi} \right) = \frac{-1}{(2\pi)^3} \int_{\mathbb{R}^3} \nabla \otimes \frac{i\mathbf{k}}{k^4} e^{i\mathbf{k}\cdot\mathbf{r}} d\mathbf{k},$$

which, expanding by the product rule, gives us

$$\nabla \otimes \nabla \left(\frac{r}{8\pi} \right) = \frac{-1}{(2\pi)^3} \int_{\mathbb{R}^3} \left(\nabla \otimes \frac{i\mathbf{k}}{k^4} \right) e^{i\mathbf{k}\cdot\mathbf{r}} + \frac{i\mathbf{k}}{k^4} \otimes \nabla e^{i\mathbf{k}\cdot\mathbf{r}} d\mathbf{k}.$$

Noting that $\nabla \otimes \frac{i\mathbf{k}}{k^4} = 0$ and $\nabla e^{i\mathbf{k}\cdot\mathbf{r}} = i\mathbf{k} e^{i\mathbf{k}\cdot\mathbf{r}}$, we obtain our last key result

$$\nabla \otimes \nabla \left(\frac{r}{8\pi} \right) = \frac{1}{(2\pi)^3} \int_{\mathbb{R}^3} \frac{\mathbf{k} \otimes \mathbf{k}}{k^4} e^{i\mathbf{k}\cdot\mathbf{r}} d\mathbf{k}.\tag{2.2.6}$$

Now, we shall return to our initial problem, as given in eq. (2.2.1), where we will find closed-form expressions for the transformed pressure and velocity fields. Subsequently, the key results we derived will be applied, allowing us to compute the analytic solutions to the original problem.

Taking the divergence of eq. (2.2.1), we obtain a Poisson equation [22] for the pressure

$$\begin{aligned}\nabla \cdot (\mu \nabla^2 \mathbf{u} - \nabla p) &= \nabla \cdot (-\mathbf{F} \delta(\mathbf{r})); \\ \nabla^2 \mathbf{u} &= 0, \\ \implies \nabla^2 p &= \nabla (\mathbf{F} \delta(\mathbf{r})).\end{aligned}$$

Fourier transforming, applying the derivative property and once again using the definition of the Dirac delta, we get

$$\begin{aligned}\nabla^2 \hat{p}(\mathbf{k}) &= \nabla (\mathcal{F}[\mathbf{F} \delta(\mathbf{r})]), \\ &= i\mathbf{k} \int_{\mathbb{R}^3} \mathbf{F} \delta(\mathbf{r}) e^{i\mathbf{k} \cdot \mathbf{r}} d\mathbf{r}, \\ \implies (i\mathbf{k})^2 \hat{p}(\mathbf{k}) &= i\mathbf{k} (\mathbf{F} e^{i\mathbf{k} \cdot \mathbf{0}}), \\ \implies \hat{p}(\mathbf{k}) &= -i \frac{\mathbf{k} \cdot \mathbf{F}}{k^2}.\end{aligned}\tag{2.2.7}$$

Using this expression, we will be able to transform the initial Stokes problem (2.2.1), eliminate pressure, and thus deduce a closed-form expression for the velocity field.

Under the Fourier transformation, using the same methodology as above, eq. (2.2.1) becomes

$$\begin{aligned}\mu \nabla^2 \hat{\mathbf{u}}(\mathbf{k}) - \nabla \hat{p}(\mathbf{k}) &= \mathcal{F}[-\mathbf{F} \delta(\mathbf{r})], \\ \implies \mu(i\mathbf{k})^2 \hat{\mathbf{u}}(\mathbf{k}) - i\mathbf{k} \hat{p}(\mathbf{k}) &= -\mathbf{F}, \\ \implies \hat{\mathbf{u}}(\mathbf{k}) &= \frac{1}{\mu k^2} (\mathbf{F} - i\mathbf{k} \hat{p}(\mathbf{k})).\end{aligned}$$

Hence, by substituting in eq. (2.2.7), the transformed velocity field is

$$\hat{\mathbf{u}}(\mathbf{k}) = \frac{1}{\mu k^2} \left(\mathbf{F} - \frac{\mathbf{k}(\mathbf{k} \cdot \mathbf{F})}{k^2} \right).\tag{2.2.8}$$

To complete the derivation, we first need to apply the inverse Fourier transform to these two expressions. Namely, eq. (2.2.7) and eq. (2.2.8) become

$$\mathcal{F}^{-1} [\hat{p}(\mathbf{k})] = p(\mathbf{r}) = \frac{1}{(2\pi)^3} \int_{\mathbb{R}^3} -i \frac{\mathbf{k} \cdot \mathbf{F}}{k^2} e^{i\mathbf{k} \cdot \mathbf{r}} d\mathbf{k};\tag{2.2.9}$$

$$\mathcal{F}^{-1} [\hat{\mathbf{u}}(\mathbf{k})] = \mathbf{u}(\mathbf{r}) = \frac{1}{(2\pi)^3} \int_{\mathbb{R}^3} \frac{1}{\mu k^2} \left(\mathbf{F} - \frac{\mathbf{k}(\mathbf{k} \cdot \mathbf{F})}{k^2} \right) e^{i\mathbf{k} \cdot \mathbf{r}} d\mathbf{k},\tag{2.2.10}$$

respectively. Writing eq. (2.2.9) as

$$p(\mathbf{r}) = -\mathbf{F} \cdot \frac{i}{(2\pi)^3} \int_{\mathbb{R}^3} \frac{\mathbf{k}}{k^2} e^{i\mathbf{k} \cdot \mathbf{r}} d\mathbf{k},$$

we note that the right-hand side contains the precise identity we obtained in eq. (2.2.4).

As such, substituting this in, we derive the final solution for the pressure

$$\begin{aligned} p(\mathbf{r}) &= -\mathbf{F} \cdot \nabla \left(\frac{1}{4\pi r} \right), \\ &= \frac{\mathbf{F} \cdot \mathbf{r}}{4\pi r^3}. \end{aligned}$$

For eq. (2.2.10), we first decompose into the two integrals

$$\mathbf{u}(\mathbf{r}) = \frac{\mathbf{F}}{\mu (2\pi)^3} \int_{\mathbb{R}^3} \frac{1}{k^2} e^{ik \cdot \mathbf{r}} d\mathbf{k} - \frac{1}{\mu (2\pi)^3} \int_{\mathbb{R}^3} \frac{\mathbf{k} (\mathbf{k} \cdot \mathbf{F})}{k^4} e^{ik \cdot \mathbf{r}} d\mathbf{k}.$$

In the first of these terms, the integral is exactly that which we found in eq. (2.2.5). For the second term, we apply the tensor identity $\mathbf{k} (\mathbf{k} \cdot \mathbf{F}) = \mathbf{F} \cdot (\mathbf{k} \otimes \mathbf{k})$ [22] and notice that the resulting integral aligns with our result from eq. (2.2.6). Substituting and simplifying, we find

$$\begin{aligned} \mathbf{u}(\mathbf{r}) &= \frac{\mathbf{F}}{\mu} \frac{1}{4\pi r} - \frac{\mathbf{F}}{\mu} \frac{1}{(2\pi)^3} \int_{\mathbb{R}^3} \frac{\mathbf{k} \otimes \mathbf{k}}{k^4} e^{ik \cdot \mathbf{r}} d\mathbf{k}, \\ &= \frac{\mathbf{F}}{\mu} \left(\frac{1}{4\pi r} - \nabla \otimes \nabla \left(\frac{r}{8\pi} \right) \right), \\ &= \frac{\mathbf{F}}{4\mu\pi} \left(\frac{1}{r} - \frac{1}{2} \nabla \otimes \left(\frac{\mathbf{r}}{r} \right) \right). \end{aligned}$$

In order to simplify the tensor product term, we note that one may write $\mathbf{r}/r = (x/r, y/r, z/r)$ and therefore, in Einstein notation, we have

$$\begin{aligned} \frac{\partial}{\partial x_j} \left(\frac{x_i}{r} \right) &= \frac{\delta_{ij}}{r} - \frac{x_i x_j}{r^3}, \\ \implies \nabla \otimes \left(\frac{\mathbf{r}}{r} \right) &= \frac{\mathbf{I}}{r} - \frac{\mathbf{r} \otimes \mathbf{r}}{r^3}. \end{aligned}$$

Hence, using this and noting that we can always write a vector in the form $\mathbf{F} = \mathbf{I}\mathbf{F}$ [22], where \mathbf{I} is the identity matrix, we finally deduce that

$$\begin{aligned} \mathbf{u}(\mathbf{r}) &= \frac{\mathbf{F}}{4\mu\pi} \left(\frac{1}{r} - \frac{1}{2} \left(\frac{\mathbf{I}}{r} - \frac{\mathbf{r} \otimes \mathbf{r}}{r^3} \right) \right), \\ &= \frac{\mathbf{F}}{8\mu\pi r} \left(2\mathbf{I} - \left(\mathbf{I} - \frac{\mathbf{r} \otimes \mathbf{r}}{r^2} \right) \right), \\ &= \frac{\mathbf{F}}{8\mu\pi r} \left(\mathbf{I} + \frac{\mathbf{r} \otimes \mathbf{r}}{r^2} \right). \end{aligned}$$

We can write this velocity solution as $\mathbf{u}(\mathbf{r}) = \mathbf{F} \cdot \mathbf{T}(\mathbf{r})$, where

$$\mathbf{T}(\mathbf{r}) = \frac{1}{8\mu\pi r} \left(\mathbf{I} + \frac{\mathbf{r} \otimes \mathbf{r}}{r^2} \right), \quad (2.2.11)$$

is the Green's function of Stokes flow, otherwise known as the Oseen–Burgers tensor [25] or, rather aptly—a Stokeslet [7].

Thus, we have found the closed-form analytic solution to our point-particle problem

$$\begin{aligned} p(\mathbf{r}) &= \mathbf{F} \cdot \frac{\mathbf{r}}{4\pi r^3}, \\ \mathbf{u}(\mathbf{r}) &= \mathbf{F} \cdot \mathbf{T}(\mathbf{r}). \end{aligned} \quad (2.2.12)$$

Taking $\mathbf{r} \rightarrow \infty$, one can note that $p, \mathbf{u} \rightarrow 0$, confirming that our desired boundary conditions are satisfied.

2.3 Forming a particle cloud

In section 2.1, we introduced the linearity property of the Stokes equations and discussed how this could be exploited to solve complex systems. We will now use linearity to establish a premise for simulation, developing the methodology established by Nitsche and Batchelor in [27], and inspired by the results presented by Metzger, Nicolas and Guazzelli in [25].

During our derivation of the Stokeslet, we determined how a force, \mathbf{F} , acting through a point-particle affected the flow in a Stokes regime. We now specify this force to be gravity, taking $\mathbf{F} = F\hat{\mathbf{e}}_g$, where $\hat{\mathbf{e}}_g$ is the downwards facing unit vector. We consider this particle to be in an infinite, low Reynolds number fluid of viscosity μ , which has zero velocity as $\mathbf{r} \rightarrow \infty$ [25]. We say that the particle in question—in the absence of additional forces—reaches a terminal downwards speed of U_0 and note that the flow anywhere else in the fluid can be calculated directly by eq. (2.2.12).

Now, we imagine a scenario in which three of these identical particles are placed at arbitrary positions, \mathbf{r}_2 , \mathbf{r}_3 and \mathbf{r}_4 . Due to the superposition principle, the resultant flow at some position, \mathbf{r}_1 , is determined by summing the Stokeslet contributions from each of these particles. In fig. 2.2, we can see how the flow at \mathbf{r}_1 is independently affected by its relative position to each of the three forces.

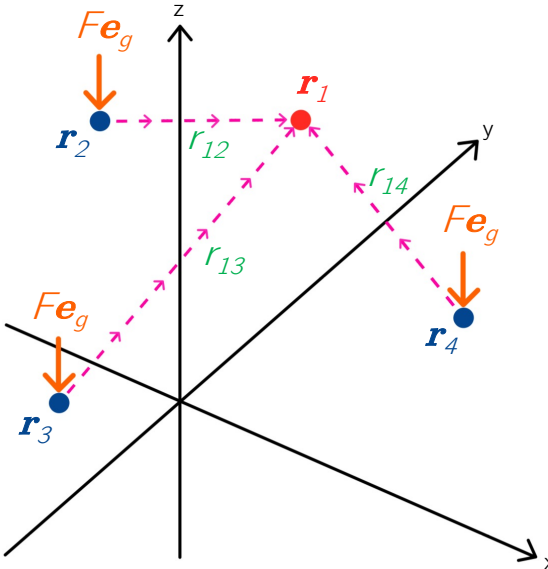


Figure 2.2: Visualisation of the superposition principle. The flow at \mathbf{r}_1 is determined by summing the Stokeslets which arise from the three gravitational point-forces at \mathbf{r}_2 , \mathbf{r}_3 and \mathbf{r}_4 .

Explicitly, the contribution from one particle is given directly by eq. (2.2.12). We then add this to U_0 , to ensure the terminal speed condition is attained at infinity.

It is clear that this process can be iterated for any arbitrary number of particles, say N_0 . Hence, we can state, for $i \in \{1, \dots, N_0\}$, the velocity at particle i is given by

$$\mathbf{u}(\mathbf{r}_i) = U_0 + F\hat{\mathbf{e}}_g \cdot \sum_{i \neq j} \mathbf{T}(\mathbf{r}_{ij}), \quad (2.3.1)$$

where $\mathbf{r}_{ij} = \mathbf{r}_i - \mathbf{r}_j$ is the vector difference between particles i and j [25], and $\mathbf{T}(\cdot)$ is the Stokeslet, from eq. (2.2.11). As in [25], we note that as the particles are identical, we can choose a frame of reference which moves with a speed of U_0 , subsequently eliminating the term without losing any information regarding dynamics.

Next, in order to remove any dependency on physical parameters, we will non-dimensionalise the system. We consider a scenario wherein N_0 particles are scattered randomly within a sphere of radius R_0 , forming a ‘cloud’. In [14], Ekiel-Jeżewska, Metzger and Guazzelli use statistical methodology to determine that the average fluid speed within such a sphere is given by

$$\bar{u} = \frac{N_0 F}{5\pi\mu R_0}.$$

Thus, we incorporate this into the non-dimensionalisation, taking

$$\mathbf{u}(\mathbf{r}_i) = \frac{N_0 F}{5\pi\mu R_0} \hat{\mathbf{u}}(\mathbf{r}_i); \quad \mathbf{r}_i = R_0 \hat{\mathbf{r}}_i; \quad r_i = R_0 \hat{r}_i,$$

where the hats represent the new non-dimensional values. With this, eq. (2.3.1) becomes

$$\begin{aligned} \mathbf{u}(\mathbf{r}_i) &= F\hat{\mathbf{e}}_g \cdot \sum_{i \neq j} \frac{1}{8\mu\pi r_{ij}} \left(\mathbf{I} + \frac{\mathbf{r}_{ij} \otimes \mathbf{r}_{ij}}{r_{ij}^2} \right), \\ \implies \frac{N_0 F}{5\pi\mu R_0} \hat{\mathbf{u}}(\mathbf{r}_i) &= F\hat{\mathbf{e}}_g \cdot \sum_{i \neq j} \frac{1}{8\pi\mu R_0 \hat{r}_{ij}} \left(\mathbf{I} + \frac{R_0^2}{R_0^2} \frac{\hat{\mathbf{r}}_{ij} \otimes \hat{\mathbf{r}}_{ij}}{\hat{r}_{ij}^2} \right), \\ \implies \hat{\mathbf{u}}(\mathbf{r}_i) &= \frac{5}{8N_0} \sum_{i \neq j} \frac{1}{\hat{r}_{ij}} \left(\mathbf{I} + \frac{\hat{\mathbf{r}}_{ij} \otimes \hat{\mathbf{r}}_{ij}}{\hat{r}_{ij}^2} \right) \cdot \hat{\mathbf{e}}_g, \end{aligned}$$

giving us a system which solely relies upon our choice of N_0 . Henceforth, this will form the basis of our simulations, but we first need to extract the explicit system of differential equations.

Dropping hats and writing $\mathbf{r}_{ij} = (x_i - x_j, y_i - y_j, z_i - z_j)$, the components of the system become

$$\begin{aligned} \frac{dx_i}{dt} &= \frac{5}{8N_0} \sum_{i \neq j} \frac{1}{r_{ij}} \left(1 + \frac{(x_i - x_j)^2}{r_{ij}^2}, \frac{(x_i - x_j)(y_i - y_j)}{r_{ij}^2}, \frac{(x_i - x_j)(z_i - z_j)}{r_{ij}^2} \right) \cdot \hat{\mathbf{e}}_g, \\ \frac{dy_i}{dt} &= \frac{5}{8N_0} \sum_{i \neq j} \frac{1}{r_{ij}} \left(\frac{(y_i - y_j)(x_i - x_j)}{r_{ij}^2}, 1 + \frac{(y_i - y_j)^2}{r_{ij}^2}, \frac{(y_i - y_j)(z_i - z_j)}{r_{ij}^2} \right) \cdot \hat{\mathbf{e}}_g, \\ \frac{dz_i}{dt} &= \frac{5}{8N_0} \sum_{i \neq j} \frac{1}{r_{ij}} \left(\frac{(z_i - z_j)(x_i - x_j)}{r_{ij}^2}, \frac{(z_i - z_j)(y_i - y_j)}{r_{ij}^2}, 1 + \frac{(z_i - z_j)^2}{r_{ij}^2} \right) \cdot \hat{\mathbf{e}}_g, \end{aligned}$$

which, as $\hat{\mathbf{e}}_g = (0, 0, -1)$, gives us the equations

$$\begin{aligned}\frac{dx_i}{dt} &= \frac{5}{8N_0} \sum_{i \neq j} -\frac{(x_i - x_j)(z_i - z_j)}{r_{ij}^3}, \\ \frac{dy_i}{dt} &= \frac{5}{8N_0} \sum_{i \neq j} -\frac{(y_i - y_j)(z_i - z_j)}{r_{ij}^3}, \\ \frac{dz_i}{dt} &= \frac{5}{8N_0} \sum_{i \neq j} -\left(\frac{1}{r_{ij}} + \frac{(z_i - z_j)^2}{r_{ij}^3} \right).\end{aligned}\tag{2.3.2}$$

This gives us a system of $3N_0$ ordinary differential equations, which we will computationally solve, in order to simulate the falling cloud of particles.

2.4 Simulating the cloud

To begin, we create a function to establish our initial particle cloud—which we model as N_0 particles randomly distributed within a sphere of radius R_0 , centred at the origin. This function randomly produces 3D coordinates for each particle within a cube of side length $2R_0$, centred at the origin. It then uses a mask to remove particles which lay outside the sphere of radius R_0 , and repeats this process until N_0 particles have been placed.

In Figure 2.3, we see a visualisation for the initial configuration of 2 000 particles within a sphere of dimensionless radius 1.

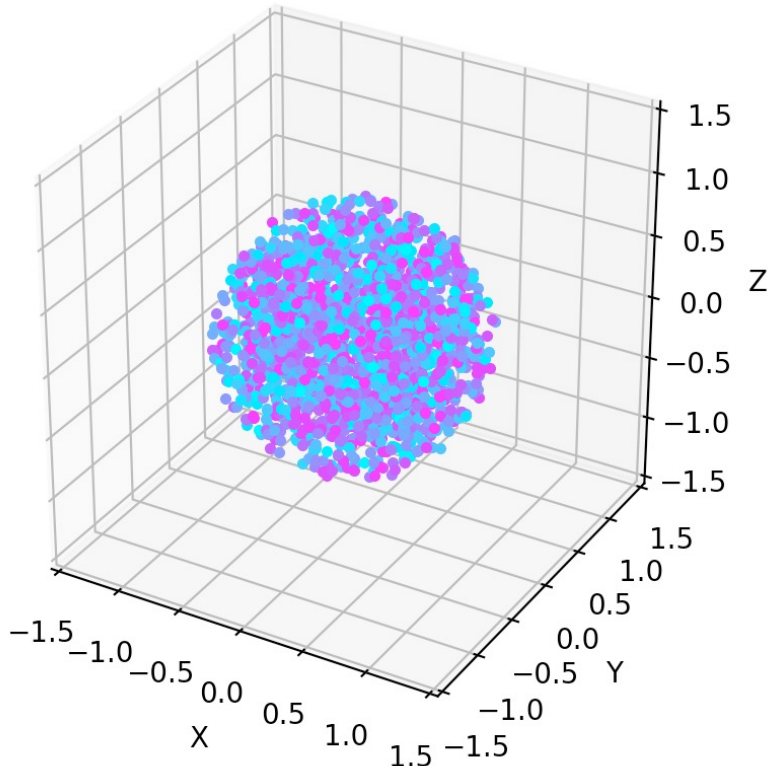


Figure 2.3: Initial particle cloud for $N_0 = 2000$, $R_0 = 1$, centred at the origin.

In order to simulate the process of our cloud falling through a viscous fluid, we solve the system given in eq. (2.3.2), using `solve_ivp` from the `scipy.integrate` package. Specifically, we use the `RK45` solver, which implements the Dormand–Prince pair of formulas [12]—an explicit Runge–Kutta numerical method of order 5(4). This means that, at each time-step, two solutions are calculated—a highly accurate solution of order five, and a computationally cheaper solution of order four. The difference between these solutions is considered the error, which subsequently determines the size of the next time-step. This adaptive time-stepping increases the efficiency of our computation, whilst producing a smooth, accurate solution.

We also increase computational efficiency significantly by employing `Numpy` vectorisation. Additionally, one may notice that as the separation between two particles approaches zero, their respective contributions to each of their flows grows unboundedly in magnitude. Explicitly, eq. (2.3.2) implies that as $r_{ij} \rightarrow 0$, $d\mathbf{x}/dt \rightarrow \infty$. To prevent this physical implausibility, we introduce a dimensionless manual cut-off distance of 1×10^{-6} , below which any flow contribution is set to 0. The inclusion of such a cut-off distance is justified by Machu et al. in [24], but we note it must be small enough to prevent arbitrary modifications of global behaviour.

With the initial conditions in fig. 2.3, we simulate for an elapsed time of $T = 1\,000$. We note that T is dimensionless, so we just require a value which is sufficiently large, to ensure the cloud can fully develop. In fig. 2.4, we see snapshots from the falling cloud simulation. In figs. 2.4a to 2.4b, we see that as the cloud begins to fall, the majority of the particles remain clustered together. However, gradually—and consistently—particles are lost from the top, resulting in a trailing, vertical tail.

This coincides with the original observations made by Nitsche and Batchelor in [27]. They identified closed toroidal trajectories of particles within the main volume of the cloud. The streamlines of the viscous fluid then curve around the exterior surface of the cloud. Due to small perturbations during the circular movement, many particles loop around too far and are subsequently lost from the main cloud. They are caught in the external fluid flow and thus form the particle trail. In fig. 2.5, we see a visualisation of the streamlines during this process, from the work of Guazzelli and Morris in [19].

The cloud continues to fall in this manner, with particles gradually lost in the vertical tail, for some time. Eventually, we observe the behaviour noted by Adachi, Kiriyama and Yoshioka in [1] and Machu et al. in [24]. In figs. 2.4c to 2.4d, we see a space begin to open up in the middle of the cloud, as it stretches into a torus. This is a direct consequence of the interior circulatory flow we previously described. The two vertical hemispheres of the cloud are rotating in opposite directions, and as particles are lost from the main cluster—causing a deficit of particles near the central vertical axis—they begin to slowly separate. This results in a torus of externally rotating particles. The process of this separation can be seen in fig. 2.6.

In the second image of fig. 2.6 and figs. 2.4e to 2.4f, we see that the torus begins to stretch horizontally. The density of particles at each end of the emerging major axis then begins to increase. Eventually, as in figs. 2.4g to 2.4h, the distribution of particles at each end hits a critical point and the cloud splits into smaller clusters. These clusters then begin to fall separately; the velocity contributions from particles in different clusters becomes negligible, so they essentially act independently.

These clusters then each display the same behaviour as our original cloud—albeit on a smaller scale. In figs. 2.4i to 2.4l, we see the clusters falling further, before splitting once again. This splitting process continues, resulting in a descending cascade of sub-clusters.

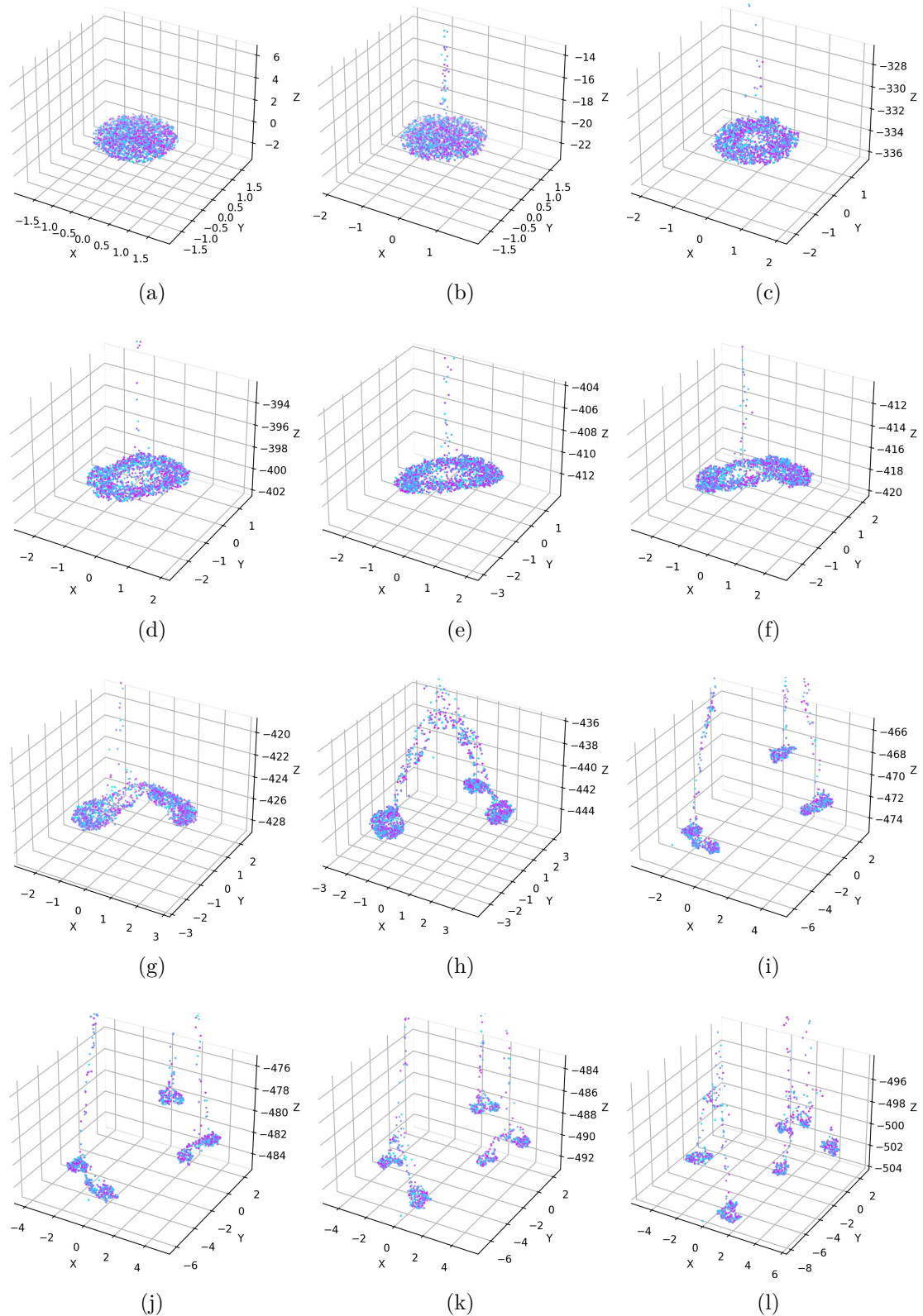


Figure 2.4: Snapshots of the falling particle cloud simulation for $N_0 = 2000$, $T = 1000$.

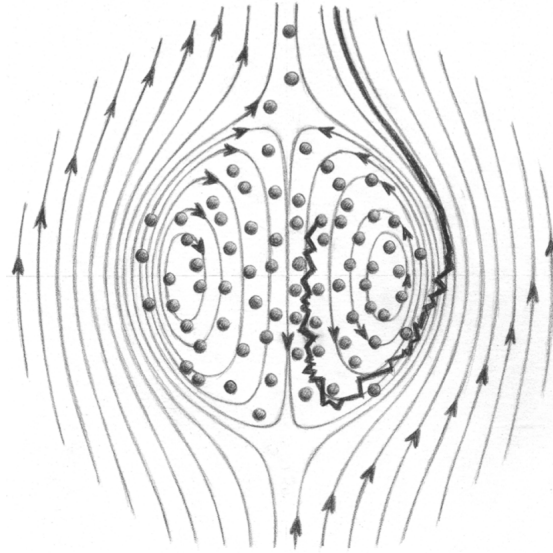


Figure 2.5: Streamline diagram demonstrating particle circulation within the falling cloud, and subsequent escape into the vertical trail. Taken from the work of Guazzelli and Morris in [19].

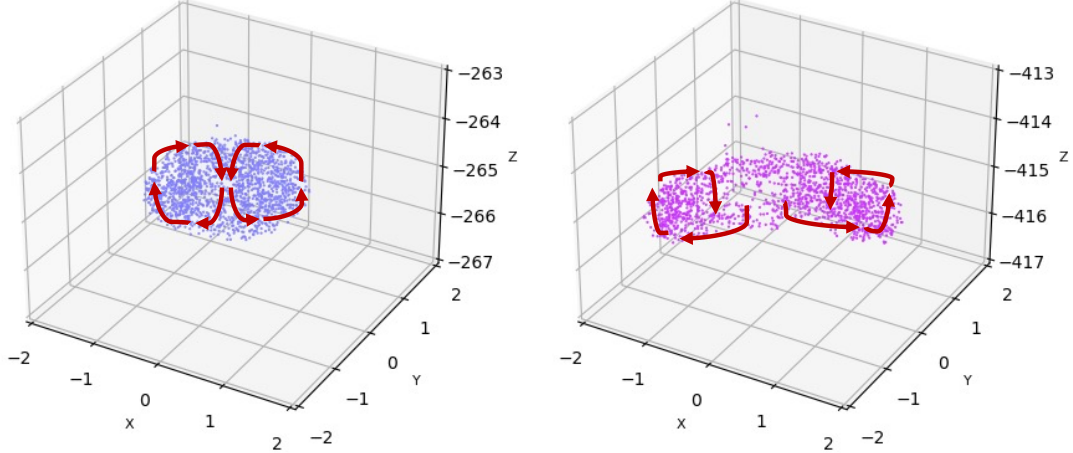


Figure 2.6: Snapshots of the falling cloud with directions of particle rotation. Toroidal particle flow can be seen, which eventually leads to the separation of the cloud into smaller clusters.

In 2007, Metzger, Nicolas and Guazzelli [25], analysed this set-up experimentally. Using a highly viscous mixture of oil and distilled water, they recorded the movement as a cloud of microscopic glass beads fell through the fluid. In fig. 2.7, we see a holistic view of our Stokes simulation, alongside the experimental results from Metzger, Nicolas and Guazzelli in [25]. We observe that our simulation has captured the true behaviour with a high level of accuracy, validating our methodology.

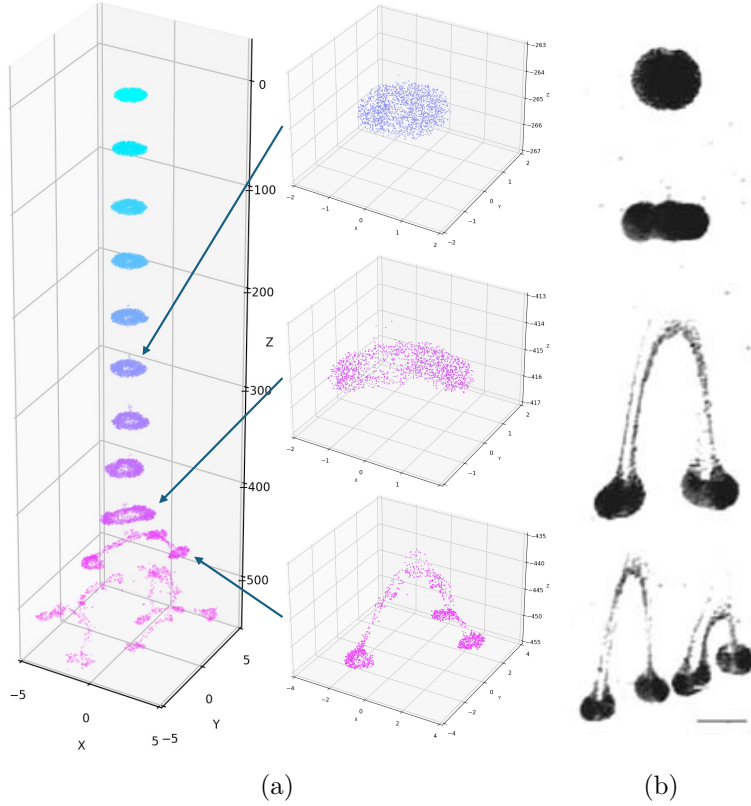


Figure 2.7: (a) Holistic view of the falling cloud simulation for $N_0 = 2\,000$.
(b) Experimental observations by Metzger, Nicolas and Guazzelli [25].

2.5 Analysing particle spread

A recurring area of interest throughout this paper is the dispersion of particles from an initial concentration. Hence, in this section, we develop and implement a framework which allows us to analyse particle spread during simulations.

First, we must specify an explicit definition of particle spread. For our falling cloud simulations, we wish to determine the radial dispersion of the cloud, as it falls through the viscous fluid.

We calculate the radial dispersion using the following algorithm:

1. We discretise the z -axis into small, non-overlapping windows. In each window, we extract the $x-y$ positions of each particle.
2. Considering first the set of x -coordinates, we find the difference between the 5th and 95th quantiles. This excludes any outlier particles and gives us an approximate width of particle spread, along the x -axis, in each window.
3. We repeat this process for the set of y -coordinates, obtaining the approximate width along the y -axis, in each window.
4. Finally, we average the widths from each axis, giving us an approximation for the radial spread, at each vertical height.

As one may expect, this produces highly volatile local behaviour, due to the discontinuous fluctuations between each vertical window. In order to approximate the behaviour smoothly, we manually implement a local linear regression estimator, as presented by Fan in [15]. This creates a smooth estimation of the average particle spread, as the cloud falls.

In fig. 2.8, we see the raw data arising from our average width algorithm, alongside the local linear regression estimate, for our $N_0 = 2\,000$ simulation.

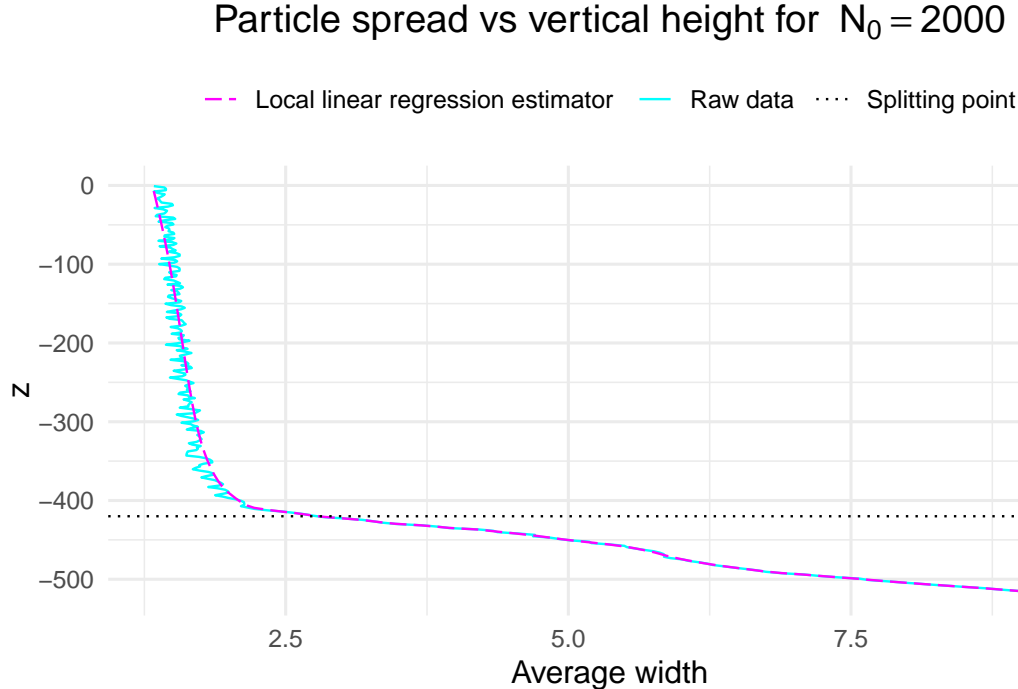


Figure 2.8: Particle spread during Stokes simulation, for $N_0 = 2\,000$. Comparison shown between the raw data and the smooth local linear regression estimate, using bandwidth $h = 0.1$ and a Gaussian kernel. The height at which the cloud splits into sub-clusters is marked for reference.

We see that the estimator follows the general behaviour of the data very accurately, whilst smoothing out the random variance which occurs. We also note the inclusion of a ‘Splitting point’, marked at $z = -420$. This indicates the vertical height at which the cloud first split into sub-clusters. We see the average width begin to increase quickly just before this point, which aligns with the torus stretching horizontally before splitting, as in figs. 2.4e to 2.4f. Once the sub-clusters emerge, the width continues to grow quickly, as these clusters separate and split further, as in figs. 2.4i to 2.4l.

With our analytic methodology established, we now evaluate the impact of different initial conditions on the particle spread. Recall that the only parameters we specify in the falling cloud simulation are N_0 and R_0 . We choose to fix R_0 and adjust N_0 , allowing us to analyse how the density of particles within the initial cloud affects the behaviour. One can note that similar observations could be made by fixing N_0 and adjusting R_0 , but the results would be less comparable, as the behaviour would occur over different dimensionless length scales.

In fig. 2.9, we see the average particle spreads—using the local linear regression estimates—for $N_0 \in \{500, 750, 1\,000, 1\,500, 2\,000\}$. The results can be categorised into two groups:

those where the cloud splits into sub-clusters, and those where it remains compact for the entire simulation duration.

Particle spread vs vertical height in Stokes simulations

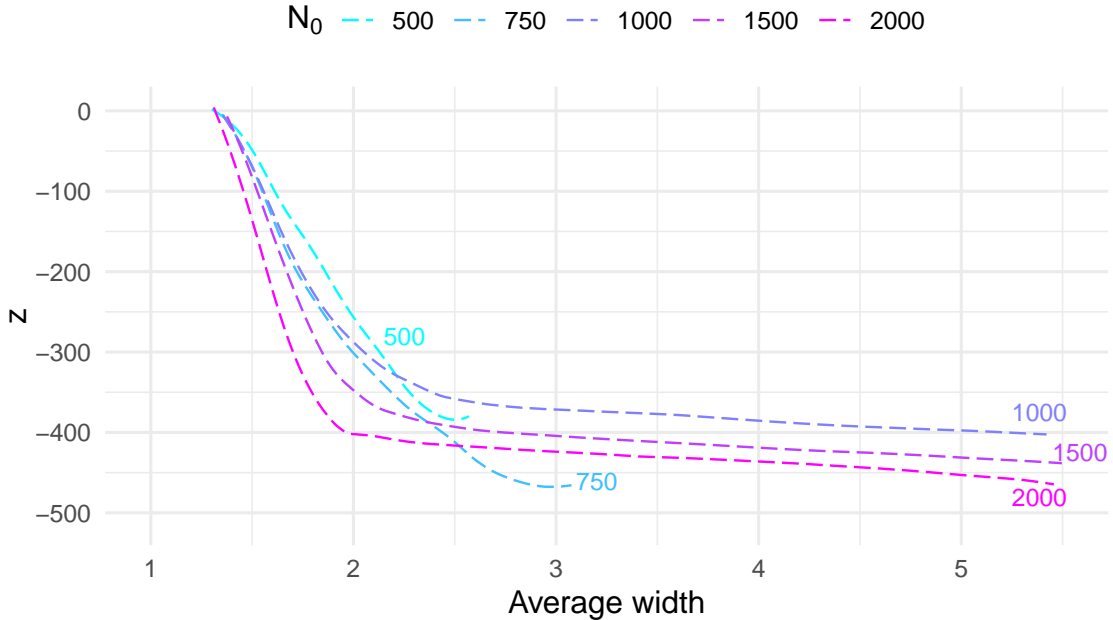


Figure 2.9: Local linear regression estimates of particle spread during Stokes simulations, for $N_0 \in \{500, 750, 1\,000, 1\,500, 2\,000\}$.

There has been extensive research into the sedimentation of smaller particle clouds in low Reynolds number fluids. The original work of Nitsche and Batchelor in 1997 [27] found that clouds with up to 320 particles maintained their structure as they fell. Latter analyses by Machu et al. [24] and Bosse et al. [5] confirmed these findings. The simulation results for $N_0 = 500, 750$ align with this behaviour. The average width gradually and consistently increases as the particles slowly separate, but we do not see the torus formation and subsequent splitting phenomena.

In further research, Machu et al. [24] confirmed that the splitting process was common for larger numbers of initial particles. Metzger, Nicolas and Guazzelli [25] performed a more comprehensive analysis of the required particle numbers for a splitting event to occur. They deduced that, whilst a splitting event could occur for a smaller numbers of particles, it was most common in simulations with $N_0 \geq 1\,000$.

This behaviour is supported by our findings in fig. 2.9, for the three simulations corresponding to $N_0 = 1\,000, 1\,500, 2\,000$. As N_0 increases, we see the particles separate at a lower rate, before a splitting event occurs. This event occurs at a lower vertical height for larger values of N_0 . This reflects the increased density of the particle cloud, as it becomes harder for them to move apart and thus takes longer for the torus to reach a critical distribution—instigating the splitting event.

It is interesting to note that, in their 2007 work, Metzger, Nicolas and Guazzelli [25] performed further numerical simulations, in which subtle perturbations were made to the initial cloud shape. They found that such perturbations, which included oblate and prolate initial shapes, were insignificant. The clouds eventually evolved towards the same torus shape, with the cloud destabilisation a robust feature.

Chapter 3

The Brinkmanlets

Thus far, we have only considered fluid disturbances which emanate from external forces acting upon the body. The flow of our viscous fluid has been otherwise unconstrained, implying the medium through which it travels is completely non-resistant; this assumption is somewhat unrealistic for many practical applications. Henceforth, we will consider non-idealised domains, with the introduction of porous media.

3.1 Darcy's law

The porosity of a medium, given by ϕ , is the proportion of a medium which is made up of empty space. For example, if a medium of volume V_M contained interconnected pores through which a fluid could travel, making up a volume of V_S , then the porosity of said medium would be

$$\phi = \frac{V_S}{V_M}.$$

In 1856, Henry Darcy formulated an empirically derived constitutive equation which models the movement of viscous fluids through such a medium. Darcy's phenomenological law is given by

$$\mathbf{q} = -\frac{K}{\mu} \nabla p, \quad (3.1.1)$$

where \mathbf{q} is the flux discharge per unit area through the medium and K is the Darcy permeability of the medium—which is a measure of how resistive a medium is to fluid flow, with SI unit m^2 . The exact measurements of K for different media is an ongoing problem, with complex experimental approaches and analytic statistical methods both being implemented, as described by Koponen, Kataja and Timonen in [21].

The velocity of a fluid is related to its flux per unit area by $\mathbf{u} = \mathbf{q}A$, where A is the cross-sectional area of the flow. Hence, the specific velocity of a fluid through a porous medium is given by

$$\mathbf{u} = -\frac{K}{\mu\phi} \nabla p, \quad (3.1.2)$$

where we divide eq. (3.1.1) by the porosity to account for the fact that only a proportion of the medium can accommodate the fluid [4]. Hence, Darcy's law states that the velocity through a porous medium is driven by the pressure gradient across the fluid.

One may note that eq. (3.1.2) relies on the assumption that the porosity of the medium is spatially homogeneous. That is, the proportion of empty space at any given cross-section of the medium is constant. Moreover, whilst initially derived from empirical observations, Darcy's law has since been formally derived using volumetric averages of the Stokes equations—as Durlofsky and Brady discuss in [13]. These properties highlight a key challenge we face when using Darcy's law—it only describes fluid flows on a macroscopic level. Specifically, it only gives us a mean fluid velocity across a uniformly permeable medium.

In fact, in 1949, Brinkman [6] observed that, on a microscopic scale, there was a qualitative difference between how viscous fluid flows were described by the Stokes equations and Darcy's law. These differences arise when the length scale of our fluid is small enough that subtle intricacies in the geometry of the medium can cause the flow to become irregular. Explicitly, finding an average velocity by assuming homogeneous permeability becomes physically uninformative.

3.2 The Brinkman equations

To address this apparent disparity, Brinkman proposed a new description of incompressible viscous flow, which interpolates between the Stokes equations and Darcy's law [6]. The incompressible Brinkman equations are given by

$$\begin{aligned} \mu \nabla^2 \mathbf{u} - \nabla p - \frac{\mu}{K} \mathbf{u} &= -\mathbf{F}, \\ \nabla \cdot \mathbf{u} &= 0. \end{aligned} \tag{3.2.1}$$

We observe that this is precisely what we saw in eq. (2.1.3), with an additional velocity term, $\mu \mathbf{u}/K$, arising from Darcy's law—where the porosity has been absorbed into the permeability parameter, K . Using the characteristic length and velocity scales as in section 2.1, we non-dimensionalise with the substitutions

$$\mathbf{u} = U \hat{\mathbf{u}}; \quad \nabla = \frac{1}{L} \widehat{\nabla}; \quad p = \frac{\mu U}{L} \hat{p}; \quad \mathbf{F} = \frac{\mu U}{L^2} \widehat{\mathbf{F}},$$

allowing us to write eq. (3.2.1) as

$$\frac{\mu U}{L^2} \widehat{\nabla}^2 \hat{\mathbf{u}} - \frac{\mu U}{L^2} \widehat{\nabla} \hat{p} - \frac{\mu U}{K} \hat{\mathbf{u}} = -\frac{\mu U}{L^2} \widehat{\mathbf{F}}.$$

Multiplying through by $L^2/\mu U$ and dropping hats for clarity, we obtain

$$\nabla^2 \mathbf{u} - \nabla p - \frac{L^2}{K} \mathbf{u} = -\mathbf{F}.$$

One can note that, in the absence of external forces, for fluids with very large characteristic length scales ($L^2 \gg K$), we have

$$\nabla^2 \mathbf{u} \ll \frac{L^2}{K} \mathbf{u},$$

so the pressure gradient predominantly balances the velocity, as in Darcy's law [13]. However, on very small characteristic length scales ($L^2 \ll K$), the inequality is reversed and

the pressure gradient instead balances the Laplacian of the velocity, as in the Stokes equations. In order to characterise this quantitative difference, we introduce the non-dimensional characteristic permeability parameter $\alpha^2 = L^2/K$. Using this, we finally obtain the incompressible, non-dimensional Brinkman equations

$$\begin{aligned} \nabla^2 \mathbf{u} - \nabla p - \alpha^2 \mathbf{u} &= -\mathbf{F}, \\ \nabla \cdot \mathbf{u} &= 0, \end{aligned} \tag{3.2.2}$$

where the value of α we select allows us to accurately describe viscous fluid flows through a porous medium, at all scales.

3.3 Solving the Brinkman equations

In order to obtain an analytic solution to the Brinkman equations, we develop the general methodology outlined by Cortez et al. in [9]. To begin, we consider the same scenario as in section 2.2—with a particle, placed at the origin, experiencing a force \mathbf{F} . However, in addition to being suspended in a viscous fluid body, we now consider the fluid itself to be flowing in a porous medium, aligning our scenario with a Brinkman regime. In addition, we once again impose the boundary conditions of $\mathbf{u}, p \rightarrow 0$ as $|\mathbf{r}| = r \rightarrow \infty$.

We will consider a generalised approach, allowing us to evaluate the Brinkman system in both its fundamental form—with the force on the particle acting through an infinitesimal point—as well as a more complex form, where the force is regularised.

Explicitly, we say the force takes the form $\mathbf{F}\phi_\delta(\mathbf{x})$, where \mathbf{F} is a constant vector and $\phi_\delta(\mathbf{x})$ is a blob function. A blob function can be considered a continuous approximation of the Dirac delta measure.

If we consider the Dirac delta function $\delta(x)$, for some scalar quantity x , the blob function which approximates this takes the form of an extremely narrow Gaussian, centred at 0. The width of this Gaussian is determined by a parameter $\delta > 0$. The density of this Gaussian quickly goes to zero as we move away from the origin. In fig. 3.1, we see examples of these blob functions for different values of δ .

One can observe that, as the width decreases, the height of the curves increases. In fact, it should be apparent from fig. 3.1 that as the width of these curves tends to zero, corresponding to $\delta \rightarrow 0$, the height of the curves goes to infinity.

This is actually a property of blob functions: in the limit $\delta \rightarrow 0$, blob functions approach a Dirac delta distribution precisely. Furthermore, this result coincides with another key characteristic of blob functions, which is that, as with a Dirac delta measure, they integrate to unity over the real numbers.

In 3D, this property is expressed as

$$\int_{\mathbb{R}^3} \phi_\delta(\mathbf{x}) d\mathbf{x} = 1. \tag{3.3.1}$$

For our model, we wish to consider the blob function in a spherical, axisymmetric regime. This is to ensure that the impact on the flow is solely dependent on the radial distance from the force. Hence, considering ϕ_δ as a radial function only, eq. (3.3.1), in spherical coordinates, becomes

$$\int_0^\infty \int_0^{2\pi} \int_0^\pi \phi_\delta(r) r^2 \sin \theta d\theta d\varphi dr = 1.$$

Scalar blob functions with the Dirac delta function

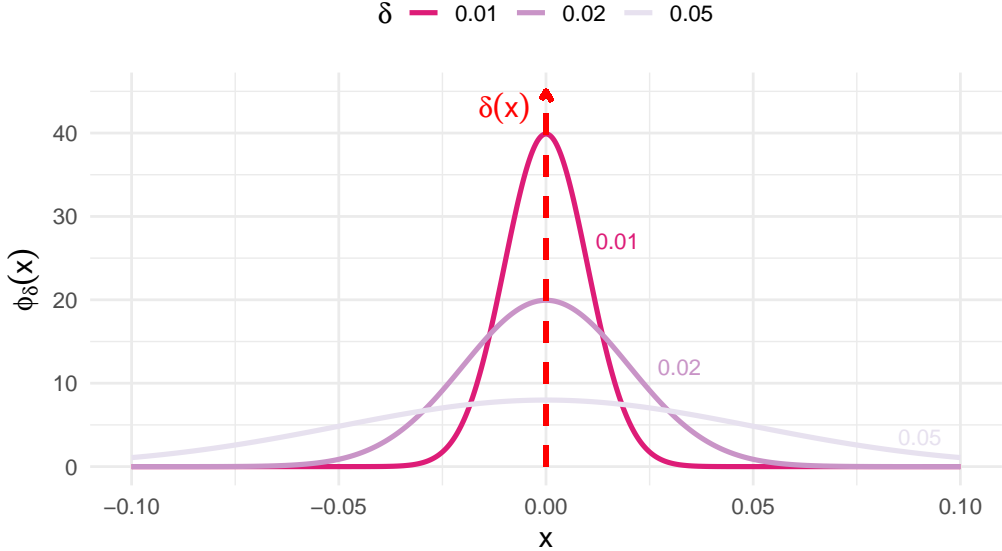


Figure 3.1: Blob functions for different width parameters, δ . Each function is given by the probability density function of a Gaussian distribution with variance δ^2 . The Dirac delta function is shown, for comparison.

Pulling out constants and simplifying, we subsequently obtain the integral which any valid spherical blob function must satisfy. This is given by

$$\int_0^\infty r^2 \phi_\delta(r) \int_0^{2\pi} 2 d\varphi dr = 1,$$

$$\implies 4\pi \int_0^\infty r^2 \phi_\delta(r) dr = 1.$$

With our premise established, we begin with the non-dimensional Brinkman equations (3.2.2). Taking the divergence of both sides, we obtain

$$\nabla \cdot (\nabla^2 \mathbf{u}(r) - \nabla p - \alpha^2 \mathbf{u}(r)) = \nabla \cdot (-\mathbf{F} \phi_\delta(r)),$$

which, due to our incompressibility assumption ($\nabla \cdot \mathbf{u} = 0$), reduces to

$$\nabla^2 p = \mathbf{F} \cdot \nabla \phi_\delta(r), \quad (3.3.2)$$

where we can pull out \mathbf{F} , as it is a constant vector.

Now, as in [9], we implicitly define a regularised approximation to the Green's function—which will henceforth be referred to as a regularised Green's function—for this system. We denote the regularised Green's function $G_\delta(r)$ and define it as the solution to the equation

$$\nabla^2 G_\delta(r) = \phi_\delta(r),$$

with the boundary condition $G_\delta(r) \rightarrow 0$ as $r \rightarrow \infty$. That is, the Laplacian of the regularised Green's function is equal to the blob function, $\phi_\delta(r)$.

Using this relation, we can write eq. (3.3.2) as

$$\begin{aligned}\nabla^2 p &= \mathbf{F} \cdot \nabla (\nabla^2 G_\delta(r)), \\ \implies \nabla^2 p &= \nabla^2 (\mathbf{F} \cdot \nabla G_\delta(r)).\end{aligned}$$

Due to the linearity of the Laplacian, we can express this as

$$\begin{aligned}\nabla^2 (p - \mathbf{F} \cdot \nabla G_\delta(r)) &= 0, \\ \implies p - \mathbf{F} \cdot \nabla G_\delta(r) &= h(\mathbf{r}),\end{aligned}$$

for some harmonic function, $h(\mathbf{r})$. As $G_\delta(r)$, $p \rightarrow 0$ as $r \rightarrow \infty$, we thus have that $h(\mathbf{r})$ also vanishes at infinity. We now prove that $h(\mathbf{r})$ must hence be identically zero.

Proof.

As $h(\mathbf{r}) \rightarrow 0$ as $|\mathbf{r}| = r \rightarrow \infty$, we can state that, for all $\varepsilon > 0$, there exists $R > 0$ such that $|h(\mathbf{r})| < \varepsilon$, for all $r > R$. That is, for $r > R$, $h(\mathbf{r})$ is bounded.

Now, consider the complement of this input space, namely—the closed ball, with radius R , centred at the origin. As $h(\mathbf{r})$ is a harmonic function and this closed ball is a compact set, the maximum principle for harmonic functions states that $|h(\mathbf{r})|$ must attain its maximum over this set when $r = R$. That is, $h(\mathbf{r})$ is bounded in this closed ball.

Hence, it follows that $h(\mathbf{r})$ is bounded for all \mathbf{r} . Thus, Liouville's theorem for harmonic functions states that $h(\mathbf{r})$ must be constant.

Finally, as $h(\mathbf{r})$ is constant, the condition that $h(\mathbf{r}) \rightarrow 0$ as $r \rightarrow \infty$ implies that $h(\mathbf{r})$ must be identically zero. \square

With this identity, we have that

$$\begin{aligned}p - \mathbf{F} \cdot \nabla G_\delta(r) &= 0, \\ \implies p &= \mathbf{F} \cdot \nabla G_\delta(r), \\ \implies \nabla p &= (\mathbf{F} \cdot \nabla) \nabla G_\delta(r).\end{aligned}$$

Substituting this back into the non-dimensional Brinkman equations (3.2.2), we get

$$\nabla^2 \mathbf{u}(\mathbf{r}) - (\mathbf{F} \cdot \nabla) \nabla G_\delta(r) - \alpha^2 \mathbf{u}(\mathbf{r}) = -\mathbf{F} \phi_\delta(r),$$

which finally, rearranging and using our definition of $G_\delta(r)$, gives us the equation

$$(\nabla^2 - \alpha^2) \mathbf{u}(\mathbf{r}) = (\mathbf{F} \cdot \nabla) \nabla G_\delta(r) - \mathbf{F} \nabla^2 G_\delta(r). \quad (3.3.3)$$

We note that the linear operator on the left-hand side of this equation is representative of a modified Helmholtz equation [3]. Hence, as in [9], we implicitly define another radial function, $B_\delta(r)$, as a solution to the inhomogeneous modified Helmholtz equation with source term $G_\delta(r)$. Explicitly, this is a function which satisfies

$$(\nabla^2 - \alpha^2) B_\delta(r) = G_\delta(r),$$

with the same boundary condition that $B_\delta(r) \rightarrow 0$ as $r \rightarrow \infty$.

Consequently, we can replace $G_\delta(r)$ with $B_\delta(r)$ in eq. (3.3.3), allowing us to obtain the representation formula

$$\mathbf{u}(\mathbf{r}) = (\mathbf{F} \cdot \nabla) \nabla B_\delta(r) - \mathbf{F} \nabla^2 B_\delta(r). \quad (3.3.4)$$

We now consider the first term of the right-hand side, and note that it represents the directional derivative of the function $\nabla B_\delta(r)$. As $B_\delta(r)$ is a solely radial function, we can write $\nabla B_\delta(r) = B'_\delta(r)$ and thus, in spherical coordinates, the directional derivative becomes

$$\begin{aligned} (\mathbf{F} \cdot \nabla) \nabla B_\delta(r) &= F_r B''_\delta(r) \hat{\mathbf{e}}_r + \frac{F_\theta}{r} B'_\delta(r) \hat{\mathbf{e}}_\theta + \frac{F_\varphi}{r} B'_\delta(r) \hat{\mathbf{e}}_\varphi, \\ &= \frac{B'_\delta(r)}{r} (F_r \hat{\mathbf{e}}_r + F_\theta \hat{\mathbf{e}}_\theta + F_\varphi \hat{\mathbf{e}}_\varphi) - \frac{B'_\delta(r)}{r} F_r \hat{\mathbf{e}}_r + F_r B''_\delta(r) \hat{\mathbf{e}}_r, \\ &= \frac{B'_\delta(r)}{r} \mathbf{F} + F_r \hat{\mathbf{e}}_r \left(B''_\delta(r) - \frac{B'_\delta(r)}{r} \right). \end{aligned}$$

Now, observe that one can write $F_r \hat{\mathbf{e}}_r = (\mathbf{F} \cdot \hat{\mathbf{e}}_r) \hat{\mathbf{e}}_r$, and furthermore, as $r = |\mathbf{r}|$, we have that $\hat{\mathbf{e}}_r = \mathbf{r}/r$. Combining these relations, we can express the directional derivative term as

$$\begin{aligned} (\mathbf{F} \cdot \nabla) \nabla B_\delta(r) &= \frac{B'_\delta(r)}{r} \mathbf{F} + (\mathbf{F} \cdot \hat{\mathbf{e}}_r) \hat{\mathbf{e}}_r \left(\frac{r B''_\delta(r) - B'_\delta(r)}{r} \right), \\ &= \frac{B'_\delta(r)}{r} \mathbf{F} + (\mathbf{F} \cdot \mathbf{r}) \mathbf{r} \left(\frac{r B''_\delta(r) - B'_\delta(r)}{r^3} \right). \end{aligned} \quad (3.3.5)$$

Returning to eq. (3.3.4), we now consider the second term of the right-hand side. Expanding the Laplacian in spherical coordinates, we deduce that

$$\begin{aligned} -\mathbf{F} \nabla^2 B_\delta(r) &= -\mathbf{F} \frac{1}{r} \frac{\partial^2}{\partial r^2} (r B_\delta(r)), \\ &= -\mathbf{F} \frac{1}{r} \frac{\partial}{\partial r} (B_\delta(r) + r B'_\delta(r)), \\ &= -\mathbf{F} \frac{1}{r} (B'_\delta(r) + B''_\delta(r) + r B''_\delta(r)), \\ &= -\mathbf{F} \left(\frac{2 B'_\delta(r) + r B''_\delta(r)}{r} \right). \end{aligned} \quad (3.3.6)$$

Hence, combining eqs. (3.3.4) to (3.3.6), we get that

$$\begin{aligned} \mathbf{u}(\mathbf{r}) &= \frac{B'_\delta(r)}{r} \mathbf{F} + (\mathbf{F} \cdot \mathbf{r}) \mathbf{r} \left(\frac{r B''_\delta(r) - B'_\delta(r)}{r^3} \right) - \mathbf{F} \left(\frac{2 B'_\delta(r) + r B''_\delta(r)}{r} \right), \\ &= \mathbf{F} \left(-\frac{r B''_\delta(r) + B'_\delta(r)}{r} \right) + (\mathbf{F} \cdot \mathbf{r}) \mathbf{r} \left(\frac{r B''_\delta(r) - B'_\delta(r)}{r^3} \right), \end{aligned}$$

which gives us our final equation for the Brinkman flow

$$\begin{aligned} \mathbf{u}(\mathbf{r}) &= \mathbf{F} H_1^\delta(r) + (\mathbf{F} \cdot \mathbf{r}) \mathbf{r} H_2^\delta(r); \\ H_1^\delta(r) &:= \left(-\frac{r B''_\delta(r) + B'_\delta(r)}{r} \right); \\ H_2^\delta(r) &:= \left(\frac{r B''_\delta(r) - B'_\delta(r)}{r^3} \right). \end{aligned} \quad (3.3.7)$$

Recalling that we implicitly defined $B_\delta(r)$ in terms of our unspecified blob function $\phi_\delta(r)$, the functions $H_1^\delta(r)$ and $H_2^\delta(r)$ subsequently encapsulate the regularisation of our force, \mathbf{F} . Subsequently, to obtain a full solution to this Brinkman system, we must specify an explicit form for $B_\delta(r)$.

3.4 Deriving a Brinkmanlet

To obtain the complete regularised solution, we first consider a simplification back to the fundamental system—akin to that which we used in our Stokeslet derivation. Explicitly, we take the limit $\delta \rightarrow 0$, replacing the blob function with a Dirac delta distribution. We thus obtain the fundamental solution to the Brinkman system—otherwise known as a Brinkmanlet [9]. From this solution, we will be able to directly impute the regularisation, resolving the flow for our generalised system.

Recalling our definition of the regularised Green's function, $G_\delta(r)$, we note that, in the singular regime, this can be expressed as

$$\nabla^2 G(r) = \delta(r),$$

where the δ superscript is dropped to distinguish between systems, and with the boundary condition maintained. One may observe that this is precisely the fundamental Laplace equation with a positive source term, akin to that previously seen in eq. (2.2.2). Thus, the solution is the Green's function of the Laplace equation

$$G(r) = -\frac{1}{4\pi r}.$$

With this value, in the fundamental system, our implicit definition of $B_\delta(r)$ becomes

$$(\nabla^2 - \alpha^2) B(r) = -\frac{1}{4\pi r}.$$

This resembles a modified Helmholtz equation in structure, but as we have assumed B to be a solely radial function, one can note that this actually simplifies to an ordinary differential equation.

Expanding the Laplacian in spherical coordinates and only considering the non-zero radial derivatives, we write this as

$$\begin{aligned} \frac{1}{r^2} \frac{d}{dr} \left(r^2 \frac{dB}{dr} \right) - \alpha^2 B &= -\frac{1}{4\pi r}, \\ \implies \frac{1}{r^2} \left(2rB' + r^2 B'' \right) - \alpha^2 B &= -\frac{1}{4\pi r}, \\ \implies B'' + \frac{2}{r} B' - \alpha^2 B &= -\frac{1}{4\pi r}, \end{aligned}$$

where the final line gives a solvable inhomogeneous differential equation.

We first examine the homogeneous version of this differential equation. Based on the structure of the equation, we assume an ansatz of the form $B_{\text{hom}}(r) = f(r)/r$, for some unknown function $f(r)$. Substituting this in, we obtain

$$\frac{d}{dr} \left(\frac{f'}{r} - \frac{f}{r^2} \right) + \frac{2}{r} \left(\frac{f'}{r} - \frac{f}{r^2} \right) - \alpha^2 \frac{f}{r} = 0,$$

$$\begin{aligned} &\implies \frac{f''}{r} - \frac{f'}{r^2} - \frac{f'}{r^2} + \frac{2f}{r^3} + \frac{2f'}{r^2} - \frac{2f}{r^3} - \alpha^2 \frac{f}{r} = 0, \\ &\implies f'' - \alpha^2 f = 0. \end{aligned}$$

Hence, we have $f(r) = A_1 e^{\alpha r} + A_2 e^{-\alpha r}$, giving us

$$B_{\text{hom}}(r) = \frac{A_1 e^{\alpha r} + A_2 e^{-\alpha r}}{r},$$

for some constants A_1 and A_2 . Due to our boundary condition of $B(r) \rightarrow 0$ as $r \rightarrow \infty$, we deduce that $A_1 = 0$ and thus, the final general solution to our homogeneous differential equation is

$$B_{\text{hom}}(r) = \frac{A_2 e^{-\alpha r}}{r}.$$

This solution is valid for any arbitrary constant A_2 —the value of which we will later specify, in order to simplify our complete solution.

Next, we consider the source term of the differential equation, $-1/4\pi r$. We assume a solution which matches the form of this source term, taking $B_p(r) = C/r$, where C is an unknown constant. With this, our differential equation becomes

$$\begin{aligned} \frac{2C}{r^3} + \frac{2}{r} \left(-\frac{C}{r^2} \right) - \alpha^2 \frac{C}{r} &= -\frac{1}{4\pi r}, \\ \implies -\alpha^2 \frac{C}{r} &= -\frac{1}{4\pi r}, \\ \implies C &= \frac{1}{4\pi\alpha^2}. \end{aligned}$$

Hence, the particular solution to the inhomogeneous system is given by $B_p(r) = 1/4\pi\alpha^2 r$. As a result, the complete solution for $B(r)$ is given by

$$\begin{aligned} B(r) &= B_{\text{hom}}(r) + B_p(r), \\ &= \frac{A_2 e^{-\alpha r}}{r} + \frac{1}{4\pi\alpha^2 r}, \\ &= \frac{4A_2\pi\alpha^2 e^{-\alpha r} + 1}{4\pi\alpha^2 r}. \end{aligned}$$

As previously stated, we are free to determine the form of the constant A_2 . Thus, assuming our medium is represented by a constant value of α , we take $A_2 = -1/4\pi\alpha^2$, giving us the final, simplified expression

$$B(r) = \frac{1 - e^{-\alpha r}}{4\pi\alpha^2 r}. \quad (3.4.1)$$

Using this expression, we can return to eq. (3.3.7) and determine the explicit forms of $H_1^\delta(r)$ and $H_2^\delta(r)$, in the fundamental system. We observe that the first two radial derivatives of $B(r)$ are given by

$$\begin{aligned} B'(r) &= \frac{e^{-\alpha r}}{4\pi\alpha r} - \frac{1 - e^{-\alpha r}}{4\pi\alpha^2 r^2}; \\ B''(r) &= -\frac{e^{-\alpha r}}{4\pi r} - \frac{2e^{-\alpha r}}{4\pi\alpha r^2} + \frac{1 - e^{-\alpha r}}{2\pi\alpha^2 r^3}. \end{aligned}$$

With these derivatives, our expression for the fundamental $H_1^\delta(r)$ becomes

$$\begin{aligned} H_1(r) &= \left(-\frac{rB''(r) + B'(r)}{r} \right), \\ &= -\frac{1}{r} \left(-\frac{e^{-\alpha r}}{4\pi} - \frac{2e^{-\alpha r}}{4\pi\alpha r} + \frac{1 - e^{-\alpha r}}{2\pi\alpha^2 r^2} + \frac{e^{-\alpha r}}{4\pi\alpha r} - \frac{1 - e^{-\alpha r}}{4\pi\alpha^2 r^2} \right), \\ &= -\frac{1}{r} \left(-\frac{e^{-\alpha r}}{4\pi} - \frac{e^{-\alpha r}}{4\pi\alpha r} + \frac{1 - e^{-\alpha r}}{4\pi\alpha^2 r^2} \right), \\ &= \frac{e^{-\alpha r}}{4\pi r} \left(1 + \frac{1}{\alpha r} + \frac{1}{\alpha^2 r^2} \right) - \frac{1}{4\pi\alpha^2 r^3}. \end{aligned}$$

Similarly, our expression for the fundamental $H_2^\delta(r)$ becomes

$$\begin{aligned} H_2(r) &= \left(\frac{rB''(r) - B'(r)}{r^3} \right), \\ &= \frac{1}{r^3} \left(-\frac{e^{-\alpha r}}{4\pi} - \frac{2e^{-\alpha r}}{4\pi\alpha r} + \frac{1 - e^{-\alpha r}}{2\pi\alpha^2 r^2} - \frac{e^{-\alpha r}}{4\pi\alpha r} + \frac{1 - e^{-\alpha r}}{4\pi\alpha^2 r^2} \right), \\ &= \frac{1}{r^3} \left(-\frac{e^{-\alpha r}}{4\pi} - \frac{3e^{-\alpha r}}{4\pi\alpha r} + \frac{3(1 - e^{-\alpha r})}{4\pi\alpha^2 r^2} \right), \\ &= -\frac{e^{-\alpha r}}{4\pi r^3} \left(1 + \frac{3}{\alpha r} + \frac{3}{\alpha^2 r^2} \right) + \frac{3}{4\pi\alpha^2 r^5}. \end{aligned}$$

Thus, we can state that the Brinkmanlet is given by

$$\begin{aligned} \mathbf{u}(\mathbf{r}) &= \mathbf{F}H_1(r) + (\mathbf{F} \cdot \mathbf{r}) \mathbf{r}H_2(r); \\ H_1(r) &:= \frac{e^{-\alpha r}}{4\pi r} \left(1 + \frac{1}{\alpha r} + \frac{1}{\alpha^2 r^2} \right) - \frac{1}{4\pi\alpha^2 r^3}; \\ H_2(r) &:= -\frac{e^{-\alpha r}}{4\pi r^3} \left(1 + \frac{3}{\alpha r} + \frac{3}{\alpha^2 r^2} \right) + \frac{3}{4\pi\alpha^2 r^5}. \end{aligned} \tag{3.4.2}$$

3.5 Deriving a regularised Brinkmanlet

Now, in order to obtain a regularised solution to the Brinkman equations, we must remove the singularity which occurs at $r = 0$, in eq. (3.4.2).

One approach is to define $R^2 = r^2 + \delta^2$, as outlined by Cortez et al. in [9], where δ is the width parameter of the aforementioned blob function. Our objective then becomes to replace $1/r$ with $1/\sqrt{(r^2 + \delta^2)}$, ensuring our solution is smoothly defined at the origin.

We first recall the expression (3.4.1) from the Brinkmanlet derivation

$$B(r) = \frac{1 - e^{-\alpha r}}{4\pi\alpha^2 r}.$$

To begin our regularisation process, we modify this expression by setting $r \mapsto R$, giving us

$$B_\delta(r) = \frac{1 - e^{-\alpha R}}{4\pi\alpha^2 R}.$$

Using this, we can obtain explicit expressions for $H_1^\delta(r)$ and $H_2^\delta(r)$, from eq. (3.3.7). These results will give us the regularised Brinkmanlet solution, but will also allow us to derive the regularised Green's function, $G_\delta(r)$. From this, we can obtain the corresponding blob function, $\phi_\delta(r)$, for our system—allowing us to evaluate the validity of our regularisation methodology.

Noting that the expressions for $H_1^\delta(r)$ and $H_2^\delta(r)$ depend upon the first two derivatives of $B_\delta(r)$, we begin by finding these. With our regularised expression, we deduce that

$$\begin{aligned} B'_\delta(r) &= \frac{r e^{-\alpha\sqrt{r^2+\delta^2}}}{4\pi\alpha(r^2+\delta^2)} - \frac{r(1-e^{-\alpha\sqrt{r^2+\delta^2}})}{4\pi\alpha^2(r^2+\delta^2)^{3/2}}, \\ &= \frac{r e^{-\alpha R}}{4\pi\alpha R^2} - \frac{r(1-e^{-\alpha R})}{4\pi\alpha^2 R^3}, \end{aligned}$$

and similarly

$$B''_\delta(r) = \frac{e^{-\alpha R}}{4\pi\alpha R^2} - \frac{r^2 e^{-\alpha R}}{4\pi R^3} - \frac{3r^2 e^{-\alpha R}}{4\pi\alpha R^4} - \frac{1-e^{-\alpha R}}{4\pi\alpha^2 R^3} + \frac{3r^2(1-e^{-\alpha R})}{4\pi\alpha^2 R^5}.$$

With these expressions, we first deduce the explicit form for $H_2^\delta(r)$, by

$$\begin{aligned} H_2^\delta(r) &= \left(\frac{r B''_\delta(r) - B'_\delta(r)}{r^3} \right), \\ &= \frac{1}{r^3} \left(\frac{r e^{-\alpha R}}{4\pi\alpha R^2} - \frac{r^3 e^{-\alpha R}}{4\pi R^3} - \frac{3r^3 e^{-\alpha R}}{4\pi\alpha R^4} - \frac{r(1-e^{-\alpha R})}{4\pi\alpha^2 R^3} \right. \\ &\quad \left. + \frac{3r^3(1-e^{-\alpha R})}{4\pi\alpha^2 R^5} - \frac{r e^{-\alpha R}}{4\pi\alpha R^2} + \frac{r(1-e^{-\alpha R})}{4\pi\alpha^2 R^3} \right), \\ &= \frac{1}{r^3} \left(-\frac{r^3 e^{-\alpha R}}{4\pi R^3} - \frac{3r^3 e^{-\alpha R}}{4\pi\alpha R^4} + \frac{3r^3(1-e^{-\alpha R})}{4\pi\alpha^2 R^5} \right), \\ &= -\frac{e^{-\alpha R}}{4\pi R^3} \left(1 + \frac{3}{\alpha R} + \frac{3}{\alpha^2 R^2} \right) + \frac{3}{4\pi\alpha^2 R^5}. \end{aligned}$$

We observe that this final form is analogous to the expression we obtained for the fundamental $H_2(r)$, with the radial distance, r , replaced with our regularised distance, R .

For $H_1^\delta(r)$, we first note that

$$\begin{aligned} H_1^\delta(r) &= \left(-\frac{r B''_\delta(r) + B'_\delta(r)}{r} \right), \\ &= -\frac{1}{r} \left(\frac{r e^{-\alpha R}}{4\pi\alpha R^2} - \frac{r^3 e^{-\alpha R}}{4\pi R^3} - \frac{3r^3 e^{-\alpha R}}{4\pi\alpha R^4} - \frac{r(1-e^{-\alpha R})}{4\pi\alpha^2 R^3} \right. \\ &\quad \left. + \frac{3r^3(1-e^{-\alpha R})}{4\pi\alpha^2 R^5} + \frac{r e^{-\alpha R}}{4\pi\alpha R^2} - \frac{r(1-e^{-\alpha R})}{4\pi\alpha^2 R^3} \right), \\ &= -\frac{2e^{-\alpha R}}{4\pi\alpha R^2} + \frac{r^2 e^{-\alpha R}}{4\pi R^3} + \frac{3r^2 e^{-\alpha R}}{4\pi\alpha R^4} + \frac{2(1-e^{-\alpha R})}{4\pi\alpha^2 R^3} - \frac{3r^2(1-e^{-\alpha R})}{4\pi\alpha^2 R^5}. \end{aligned}$$

Then, substituting $r^2 = R^2 - \delta^2$, we can write this as

$$\begin{aligned}
H_1^\delta(r) &= -\frac{2e^{-\alpha R}}{4\pi\alpha R^2} + \frac{(R^2 - \delta^2)e^{-\alpha R}}{4\pi R^3} + \frac{3(R^2 - \delta^2)e^{-\alpha R}}{4\pi\alpha R^4} + \frac{2(1 - e^{-\alpha R})}{4\pi\alpha^2 R^3} \\
&\quad - \frac{3(R^2 - \delta^2)(1 - e^{-\alpha R})}{4\pi\alpha^2 R^5}, \\
&= -\frac{2e^{-\alpha R}}{4\pi\alpha R^2} + \frac{R^2 e^{-\alpha R}}{4\pi R^3} + \frac{3R^2 e^{-\alpha R}}{4\pi\alpha R^4} + \frac{2(1 - e^{-\alpha R})}{4\pi\alpha^2 R^3} - \frac{3R^2(1 - e^{-\alpha R})}{4\pi\alpha^2 R^5} \\
&\quad + \delta^2 \left(-\frac{e^{-\alpha R}}{4\pi R^3} - \frac{3e^{-\alpha R}}{4\pi\alpha R^4} + \frac{3(1 - e^{-\alpha R})}{4\pi\alpha^2 R^5} \right), \\
&= \frac{e^{-\alpha R}}{4\pi R} \left(1 + \frac{1}{\alpha R} + \frac{1}{\alpha^2 R^2} \right) - \frac{1}{4\pi\alpha^2 R^3} \\
&\quad + \delta^2 \left(-\frac{e^{-\alpha R}}{4\pi R^3} \left(1 + \frac{3}{\alpha R} + \frac{3}{\alpha^2 R^2} \right) + \frac{3}{4\pi\alpha^2 R^5} \right),
\end{aligned}$$

where we remark that the coefficient of δ^2 is precisely the expression we just obtained for $H_2^\delta(r)$. That is, the final explicit form for $H_1^\delta(r)$ is

$$H_1^\delta(r) = \frac{e^{-\alpha R}}{4\pi R} \left(1 + \frac{1}{\alpha R} + \frac{1}{\alpha^2 R^2} \right) - \frac{1}{4\pi\alpha^2 R^3} + \delta^2 H_2^\delta(r).$$

Once again, this expression is analogous to the form we obtained for the fundamental $H_1(r)$, with the radial distance, r , replaced with our regularised distance, R . However, we now also see the additional regularisation term $\delta^2 H_2^\delta(r)$.

We now derive the corresponding regularised Green's function. Recall that we implicitly defined $B_\delta(r)$ as the solution to the inhomogeneous modified Helmholtz equation

$$(\nabla^2 - \alpha^2) B_\delta(r) = G_\delta(r).$$

Hence, in order to determine the regularised Green's function, we need to evaluate the left-hand side of this relation. As $B_\delta(r)$ is a solely radial function, expanding the Laplacian in spherical coordinates gives us

$$\begin{aligned}
G_\delta(r) &= \frac{1}{r^2} \frac{d}{dr} \left(r^2 B'_\delta(r) \right) - \alpha^2 B_\delta(r), \\
&= \frac{1}{r^2} \left(2r B'_\delta(r) + r^2 B''_\delta(r) \right) - \alpha^2 B_\delta(r), \\
&= \frac{2B'_\delta(r)}{r} + B''_\delta(r) - \alpha^2 B_\delta(r).
\end{aligned}$$

Subsequently, substituting the values we obtained above for $B_\delta(r)$, $B'_\delta(r)$ and $B''_\delta(r)$ gives us

$$\begin{aligned}
G_\delta(r) &= \frac{2}{r} \left(\frac{re^{-\alpha R}}{4\pi\alpha R^2} - \frac{r(1 - e^{-\alpha R})}{4\pi\alpha^2 R^3} \right) + \frac{e^{-\alpha R}}{4\pi\alpha R^2} - \frac{r^2 e^{-\alpha R}}{4\pi R^3} - \frac{3r^2 e^{-\alpha R}}{4\pi\alpha R^4} - \frac{1 - e^{-\alpha R}}{4\pi\alpha^2 R^3} \\
&\quad + \frac{3r^2(1 - e^{-\alpha R})}{4\pi\alpha^2 R^5} - \frac{1 - e^{-\alpha R}}{4\pi R},
\end{aligned}$$

$$= \frac{3e^{-\alpha R}}{4\pi\alpha R^2} - \frac{3(1 - e^{-\alpha R})}{4\pi\alpha^2 R^3} - \frac{r^2 e^{-\alpha R}}{4\pi R^3} - \frac{3r^2 e^{-\alpha R}}{4\pi\alpha R^4} + \frac{3r^2(1 - e^{-\alpha R})}{4\pi\alpha^2 R^5} - \frac{1 - e^{-\alpha R}}{4\pi R}.$$

As before, we now perform the substitution $r^2 = R^2 - \delta^2$ and collate terms by these new cofactors, which gives

$$\begin{aligned} G_\delta(r) &= \frac{3e^{-\alpha R}}{4\pi\alpha R^2} - \frac{3(1 - e^{-\alpha R})}{4\pi\alpha^2 R^3} - \frac{(R^2 - \delta^2)e^{-\alpha R}}{4\pi R^3} - \frac{3(R^2 - \delta^2)e^{-\alpha R}}{4\pi\alpha R^4} \\ &\quad + \frac{3(R^2 - \delta^2)(1 - e^{-\alpha R})}{4\pi\alpha^2 R^5} - \frac{1 - e^{-\alpha R}}{4\pi R}, \\ &= \frac{3e^{-\alpha R}}{4\pi\alpha R^2} - \frac{3(1 - e^{-\alpha R})}{4\pi\alpha^2 R^3} - \frac{e^{-\alpha R}}{4\pi R} - \frac{3e^{-\alpha R}}{4\pi\alpha R^2} + \frac{3(1 - e^{-\alpha R})}{4\pi\alpha^2 R^3} + \frac{e^{-\alpha R}}{4\pi R} \\ &\quad - \frac{1}{4\pi R} - \delta^2 \left(-\frac{e^{-\alpha R}}{4\pi R^3} - \frac{3e^{-\alpha R}}{4\pi\alpha R^4} + \frac{3(1 - e^{-\alpha R})}{4\pi\alpha^2 R^5} \right), \\ &= -\frac{1}{4\pi R} - \delta^2 \left(-\frac{e^{-\alpha R}}{4\pi R^3} \left(1 + \frac{3}{\alpha R} + \frac{3}{\alpha^2 R^2} \right) + \frac{3}{4\pi\alpha^2 R^5} \right). \end{aligned}$$

Once again, we observe that the coefficient of δ^2 is precisely the expression we obtained for $H_2^\delta(r)$. As such, the final form for the regularised Green's function is given by

$$G_\delta(r) = -\frac{1}{4\pi R} - \delta^2 H_2^\delta(r),$$

which we note—as with the regularised $H_1^\delta(r)$ and $H_2^\delta(r)$ —is analogous to the expression we obtained for the fundamental system, but with an additional $-\delta^2 H_2^\delta(r)$ term.

Finally, we can use the regularised Green's function in order to determine an explicit form for the corresponding blob function—which we can then verify satisfies our initial conditions.

Recall that we initially defined $G_\delta(r)$ as the solution to $\nabla^2 G_\delta(r) = \phi_\delta(r)$, where $\phi_\delta(r)$ is the blob function for the system. Using the explicit form for the regularised Green's function, this tell us

$$\begin{aligned} \phi_\delta(r) &= \nabla^2 \left(-\frac{1}{4\pi R} - \delta^2 H_2^\delta(r) \right), \\ &= \nabla^2 \left(-\frac{1}{4\pi R} \right) - \delta^2 \nabla^2 H_2^\delta(r), \end{aligned}$$

as the Laplacian is a linear operator. Using the substitution $R = \sqrt{r^2 + \delta^2}$ and expanding the Laplacian in spherical coordinates, we deduce that

$$\begin{aligned} \phi_\delta(r) &= \frac{1}{r^2} \frac{d}{dr} \left(r^2 \frac{d}{dr} \left(-\frac{1}{4\pi\sqrt{r^2 + \delta^2}} \right) \right) - \delta^2 \nabla^2 H_2^\delta(r), \\ &= \frac{1}{r^2} \frac{d}{dr} \left(\frac{r^3}{4\pi(r^2 + \delta^2)^{3/2}} \right) - \delta^2 \nabla^2 H_2^\delta(r), \\ &= \frac{1}{r^2} \left(\frac{12\pi r^2(r^2 + \delta^2)^{3/2} - 12\pi r^4(r^2 + \delta^2)^{1/2}}{16\pi^2(r^2 + \delta^2)^3} \right) - \delta^2 \nabla^2 H_2^\delta(r), \end{aligned}$$

$$= \frac{3(r^2 + \delta^2) - 3r^2}{4\pi(r^2 + \delta^2)^{5/2}} - \delta^2 \nabla^2 H_2(\delta r).$$

Thus, our final expression for the blob function of the system is given by

$$\phi_\delta(r) = \frac{3\delta^2}{4\pi(r^2 + \delta^2)^{5/2}} - \delta^2 \nabla^2 H_2^\delta(r),$$

where the inclusion of the function $H_2^\delta(r)$ implies that our blob function depends on the specified value of α in our medium.

In order to ensure this is a valid blob function, we must verify that it always satisfies the property we specified in section 3.3. Namely, we need to confirm that $4\pi \int_0^\infty r^2 \phi_\delta(r) dr = 1$, for all values of α and δ .

Using our expression for $\phi_\delta(r)$ and expanding the Laplacian in spherical coordinates, we have

$$\begin{aligned} 4\pi \int_0^\infty r^2 \phi_\delta(r) dr &= 4\pi \int_0^\infty \frac{3r^2 \delta^2}{4\pi(r^2 + \delta^2)^{5/2}} - r^2 \delta^2 \nabla^2 H_2^\delta(r) dr, \\ &= 3\delta^2 \int_0^\infty \frac{r^2}{(r^2 + \delta^2)^{5/2}} dr - 4\pi \delta^2 \int_0^\infty \frac{d}{dr} \left(r^2 \frac{dH_2^\delta(r)}{dr} \right) dr. \end{aligned}$$

If we first consider the second of these integrals, one can note that, by the fundamental theorem of calculus, we have

$$\int_0^\infty \frac{d}{dr} \left(r^2 \frac{dH_2^\delta(r)}{dr} \right) dr = \left[r^2 \frac{dH_2^\delta(r)}{dr} \right]_0^\infty.$$

For our regularised $H_2^\delta(r)$, we can write

$$r^2 \frac{dH_2^\delta(r)}{dr} = \frac{\alpha r^3 e^{-\alpha R}}{4\pi R^4} + \frac{3r^3 e^{-\alpha R}}{2\pi R^5} + \frac{15r^3 e^{-\alpha R}}{4\pi \alpha R^6} - \frac{15r^3 (1 - e^{-\alpha R})}{4\pi \alpha^2 R^7}.$$

Clearly, when $r = 0$, this quantity vanishes, so we only need to consider the limit as $r \rightarrow \infty$. In this limit, $R = \sqrt{r^2 + \delta^2} \rightarrow r$, so we have

$$\begin{aligned} \lim_{r \rightarrow \infty} r^2 \frac{dH_2^\delta(r)}{dr} &= \lim_{r \rightarrow \infty} \left(\frac{\alpha e^{-\alpha r}}{4\pi r} + \frac{3e^{-\alpha r}}{2\pi r^2} + \frac{15e^{-\alpha r}}{4\pi \alpha r^3} - \frac{15(1 - e^{-\alpha r})}{4\pi \alpha^2 r^4} \right), \\ &= 0. \end{aligned}$$

This tells us that the second integral always vanishes, irrespective of the values of α and δ .

We now turn our attention back to the first integral, where, assuming $\delta > 0$ is fixed for a given blob function, we perform the substitution $r = \delta \tan(u)$. This gives us $dr = \delta \sec^2(u) du$. Furthermore, we note that $r \rightarrow \infty \implies u \rightarrow \pi/2$ and $r = 0 \implies u = 0$, allowing us to express the integral as

$$3\delta^2 \int_0^\infty \frac{r^2}{(r^2 + \delta^2)^{5/2}} dr = 3\delta^2 \int_0^{\pi/2} \frac{\delta^3 \tan^2(u) \sec^2(u)}{(\delta^2 \tan^2(u) + \delta^2)^{5/2}} du,$$

where the identity $\tan^2(u) + 1 = \sec^2(u)$ gives

$$\begin{aligned} 3\delta^2 \int_0^{\frac{\pi}{2}} \frac{\delta^3 \tan^2(u) \sec^2(r)}{(\delta^2 \tan^2(u) + \delta^2)^{5/2}} du &= 3\delta^2 \int_0^{\frac{\pi}{2}} \frac{\delta^3 \tan^2(u) \sec^2(r)}{(\delta^2 \sec^2(u))^{5/2}} du, \\ &= 3 \int_0^{\frac{\pi}{2}} \sin^2(u) \cos(u) du, \\ &= [\sin^3(u)]_0^{\pi/2}, \\ &= 1. \end{aligned}$$

That is, our blob function always satisfies the specified regularisation property, for all Brinkman mediums and all width parameters.

With the validity of our blob function verified, we can finally state that the regularised solution to the Brinkman equations—otherwise known as a regularised Brinkmanlet—is given by

$$\begin{aligned} \mathbf{u}(\mathbf{r}) &= \mathbf{F}H_1^\delta(r) + (\mathbf{F} \cdot \mathbf{r}) \mathbf{r}H_2^\delta(r); \\ H_1^\delta(r) &:= \frac{e^{-\alpha R}}{4\pi R} \left(1 + \frac{1}{\alpha R} + \frac{1}{\alpha^2 R^2} \right) - \frac{1}{4\pi\alpha^2 R^3} + \delta^2 H_2^\delta(r); \\ H_2^\delta(r) &:= -\frac{e^{-\alpha R}}{4\pi R^3} \left(1 + \frac{3}{\alpha R} + \frac{3}{\alpha^2 R^2} \right) + \frac{3}{4\pi\alpha^2 R^5}, \end{aligned} \quad (3.5.1)$$

where the force which instigates the Brinkman flow is concentrated through the blob function

$$\phi_\delta(r) = \frac{3\delta^2}{4\pi(r^2 + \delta^2)^{5/2}} - \delta^2 \nabla^2 H_2^\delta(r). \quad (3.5.2)$$

In fig. 3.2, we see heatmap projections of this radial blob function, for $\delta = 0.01, 0.02$, in close proximity to the origin.

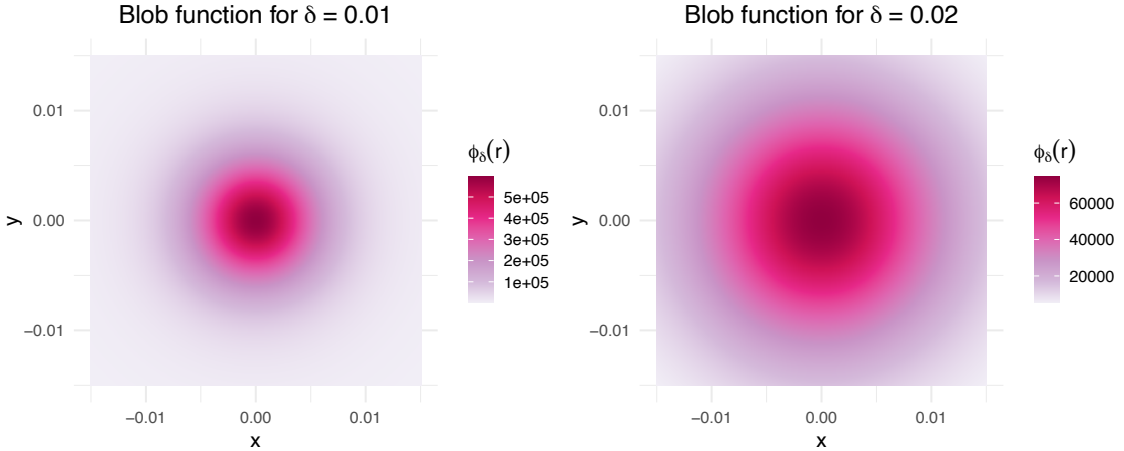


Figure 3.2: Blob function heatmaps for different width parameters, δ . Both functions determined by eq. (3.5.2).

Intuitively, as we increase the width parameter, the blob function covers a greater area around the origin. As both functions must integrate to unity over this space, we subsequently see the wider blob attain a smaller maximum. This is equivalent to the Gaussian curves flattening out as δ increased, as we saw in fig. 3.1.

In order to understand the qualitative change that arises from regularisation, we compare

the resultant Brinkman flows from a single force, placed at the origin. Taking $\mathbf{F} = (1, 1, 0)$, we obtain the fundamental Brinkman solution, using eq. (3.4.2), and the regularised Brinkman solution, using eq. (3.5.1). Using the `streamplot` function from the `matplotlib` package, we visualise a 2D projection of the arising streamlines, in fig. 3.3. The red circles demonstrate the differing concentrations of the force, in each scenario.

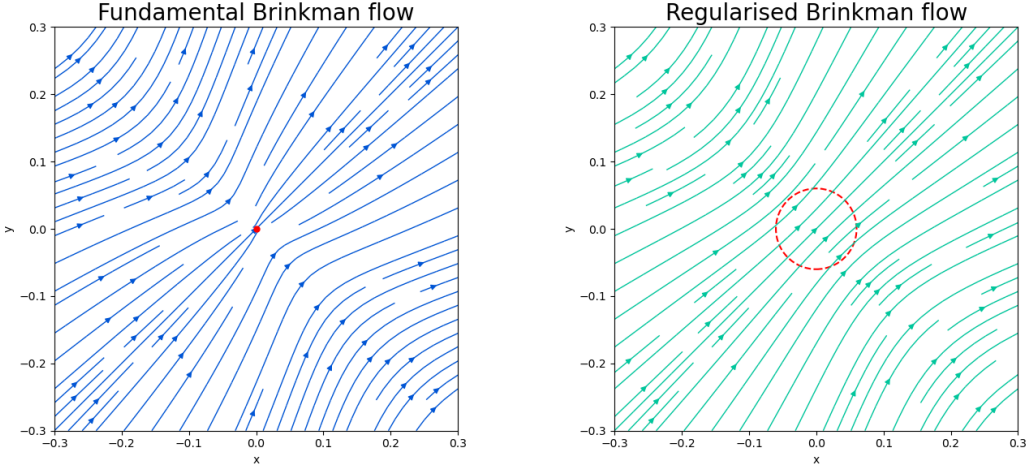


Figure 3.3: Brinkman flow streamline comparison, from fundamental and regularised forces placed at the origin, with permeability parameter $\alpha = 1$. Red circles represent the concentrations of the forces. For the regularised force, the blob function has width parameter $\delta = 0.1$.

As we would expect, the notable difference arises around the origin. In the fundamental flow, the streamlines bend quite sharply, and are more densely packed at the origin. This characterises the instability which is created by the singularity at the origin.

On the contrary, in the regularised flow, the streamlines are smoother and more evenly spaced. The smoothing effect demonstrates how the blob function has spread the concentration of the point-force over a small area.

We note that, as we move away from the origin, the streamlines in the two plots become indistinguishable. This is again to be expected—as the regularisation is only designed to remove the singularity, without affecting the general behaviour of the solution. We can thus consider the width parameter to be a smoothing factor. Increasing δ reduces the curvature about the origin, at the potential sacrifice of local information.

With solutions to the Brinkman equations established, for both a fundamental and regularised force, we can proceed with further numerical simulations. This will allow us to understand how the introduction of a porous medium affects the flow of viscous fluids.

Chapter 4

The falling Brinkmanlets

We now return to the scenario we introduced in section 2.3, wherein a spherical cloud of particles are falling under gravity in a viscous fluid. In order to align this set-up with the Brinkman regime, we now consider the viscous fluid to be flowing through a vertical porous medium, with characteristic permeability parameter α .

4.1 Forming a particle cloud II

Recalling that the non-dimensional Brinkman equations are given by

$$\begin{aligned}\nabla^2 \mathbf{u} - \nabla p - \alpha^2 \mathbf{u} &= -\mathbf{F}, \\ \nabla \cdot \mathbf{u} &= 0,\end{aligned}$$

we observe that, if we assume α is spatially homogeneous, these equations are—like the Stokes equations—linear. This assumption is justified, provided we consider the medium to have an approximately uniform porosity throughout. Due to the property of linearity, we can once again construct the particle cloud using the principle of superposition.

We note that, for the proceeding simulations, we superpose fundamental Brinkman solutions. This is to allow for direct comparison with the results we obtained in our Stokes flow simulations. Furthermore, as we are only interested in the global behaviour of the cloud, the smoothness of individual interactions on a local level is not significant to our findings.

Building upon the premise established in section 2.3, we once again consider the force acting through each particle to be $\mathbf{F} = F\hat{\mathbf{e}}_g$. The flow arising from each particle is subsequently given by the Brinkmanlet, as in eq. (3.4.2). In addition, we once again include a local cut-off distance of 1×10^{-6} , for computational feasibility.

Considering again a sphere of N_0 particles, by superposing the velocity contributions from each particle, the velocity at particle i is given by

$$\begin{aligned}\mathbf{u}(\mathbf{r}_i) &= \sum_{i \neq j} (\mathbf{F} H_1(r_{ij}) + (\mathbf{F} \cdot \mathbf{r}_{ij}) \mathbf{r}_{ij} H_2(r_{ij})) , \\ &= \sum_{i \neq j} (H_1(r_{ij}) + (\mathbf{r}_{ij} \otimes \mathbf{r}_{ij}) H_2(r_{ij})) \cdot F\hat{\mathbf{e}}_g.\end{aligned}\tag{4.1.1}$$

Once again, $\mathbf{r}_{ij} = \mathbf{r}_i - \mathbf{r}_j$ is the vector difference between particles i and j and $r_{ij} = |\mathbf{r}_{ij}|$; we also take $F = 1$ as an arbitrary constant. As our Brinkmanlet solution arises from the non-dimensional Brinkman equations, this relation is already dimensionless. That is, the viscosity, μ , of the fluid has been absorbed into the characteristic permeability parameter, α .

Our Stokes flow simulations were solely dependent upon our choices of N_0 and R_0 . This remains true, but we must now also specify a value for α . As such, we can investigate the impact of medium permeability on the behaviour of the cloud.

In order to extract the explicit system of differential equations from eq. (4.1.1), we again write $\mathbf{r}_{ij} = (x_i - x_j, y_i - y_j, z_i - z_j)$. As $\hat{\mathbf{e}}_g = (0, 0, -1)$, the components of the system can then be expressed as

$$\begin{aligned}\frac{dx_i}{dt} &= \sum_{i \neq j} -(x_i - x_j)(z_i - z_j)H_2(r_{ij}), \\ \frac{dy_i}{dt} &= \sum_{i \neq j} -(y_i - y_j)(z_i - z_j)H_2(r_{ij}), \\ \frac{dz_i}{dt} &= \sum_{i \neq j} -H_1(r_{ij}) - (z_i - z_j)^2 H_2(r_{ij}).\end{aligned}\tag{4.1.2}$$

This is another system of $3N_0$ ordinary differential equations, which we can numerically solve in order to simulate a falling cloud in a Brinkman regime.

4.2 High permeability simulations

Recall that our characteristic permeability parameter follows the relationship $\alpha^2 \propto 1/K$, where K is the specific permeability of the medium. This means that, as the porosity—and subsequently the permeability—of the medium increases, α decreases. A more intuitive way to consider the effects of α is therefore to view it as a non-dimensional resistivity parameter.

As $\alpha \rightarrow 0$, we are effectively saying that the fluid is experiencing no resistance from the medium. In fact, in this limit, the non-dimensional Brinkman equations reduce to

$$\begin{aligned}\nabla^2 \mathbf{u} - \nabla p &= -\mathbf{F}, \\ \nabla \cdot \mathbf{u} &= 0,\end{aligned}$$

which is precisely the form of the non-dimensional Stokes equations we saw in chapter 2. This is representative of the inherent interpolation of the Stokes equations within the Brinkman equations. As the resistivity of the medium becomes negligible, we are simply modelling the unrestricted flow of a viscous fluid—as with the Stokes equations.

It makes sense, therefore, to begin our Brinkman flow analysis with a validation of our methodology, by simulating the falling cloud in a low- α medium.

We establish identical initial conditions to that of section 2.4, with $N_0 = 2000$ particles randomly scattered within a sphere of dimensionless radius 1, as seen in fig. 2.3. Taking $\alpha = 0.01$, we then simulate the system given in eq. (4.1.2)—once again using the RK45 solver.

In fig. 4.1, we see a holistic view of the cloud's progression, alongside the corresponding results from our Stokes flow simulation.

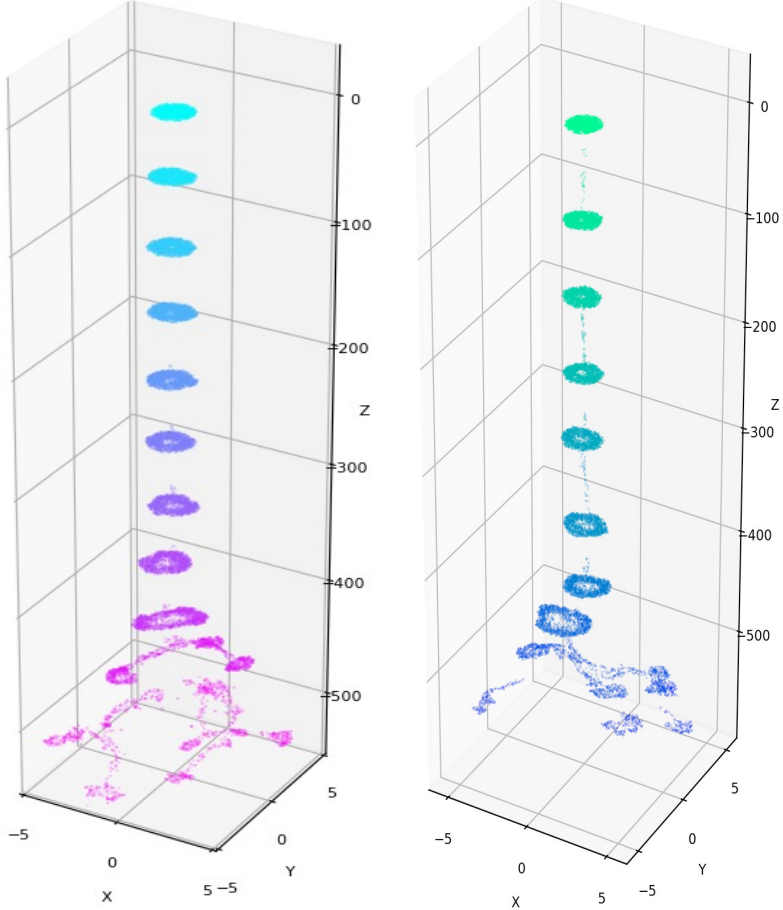


Figure 4.1: Comparative holistic overviews of the falling clouds in a Stokes regime (left) and a Brinkman regime with $\alpha = 0.01$ (right).

These results demonstrate the behaviour we expected; the general progression of the cloud is fundamentally unaffected by the low- α medium. The cloud remains compact as it falls and slowly loses particles from the top. It forms a torus, before hitting a critical distribution and splitting into sub-clusters. These clusters fall further, before splitting again.

This confirms the asymptotic alignment of the Brinkman equations with the Stokes equations, in the limit $\alpha \rightarrow 0$. We will now increase the value of α and evaluate how the cloud is affected.

4.3 Decreasing the permeability

Assuming that the viscosity remains constant, an increase in α directly models a decrease in porosity, and therefore permeability, of our medium. Previously, we discussed how, for fluids with very large characteristic length scales ($L^2 \gg K$), the Brinkman equations behaved like Darcy's law—rather than the Stokes equations. Hence, by increasing α , we expect to see qualitatively different dynamics.

In fig. 4.2, we see the results from three further simulations, where we modelled the same cloud, for $\alpha = 1, 5, 10$. The results are very interesting, and clearly demonstrate the differences between the Stokes equations and Darcy's law. For the latter two plots, we note that the particles actually spread further than is shown, but we limit the axes for visual clarity. We analyse this spread more rigorously in section 4.4.

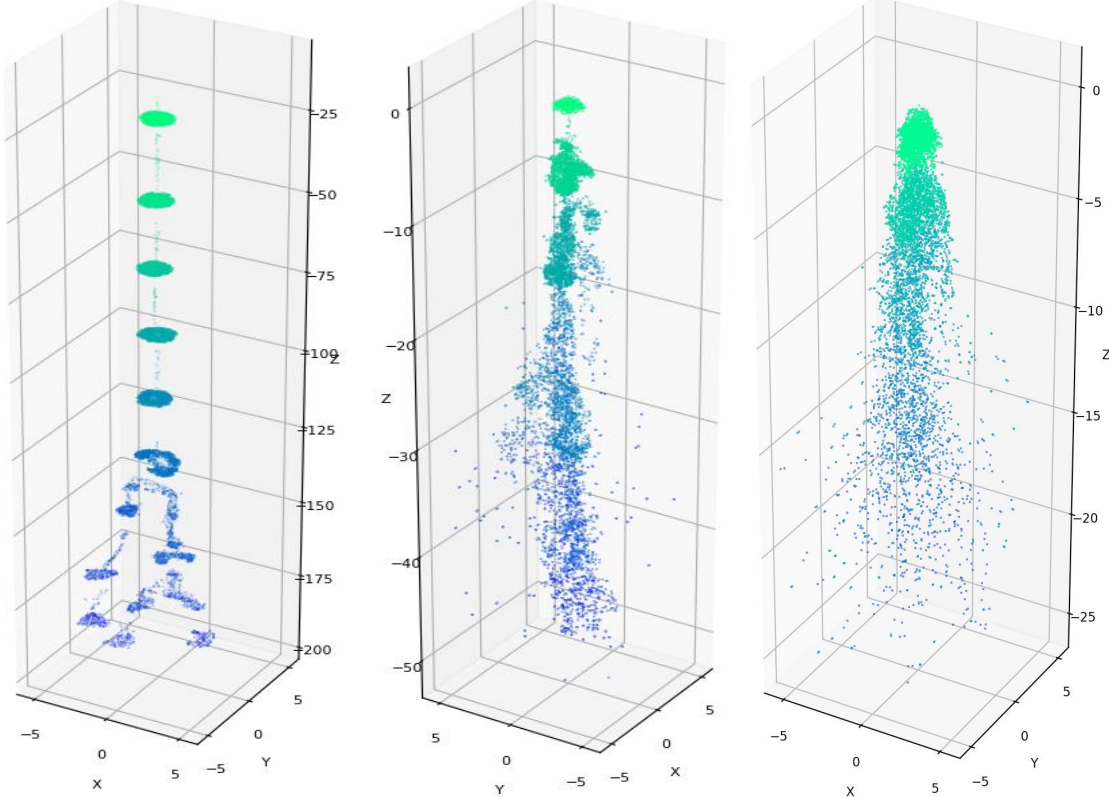


Figure 4.2: Comparative holistic overviews of the falling clouds in different Brinkman regimes, with $N_0 = 2000$ and $\alpha = 1, 5, 10$ (left to right).

For $\alpha = 1$, we have $L^2 = K$. Physically, this represents the turning point between where the Brinkman equations behave more like the Stokes equations, to being more akin to Darcy's law. If we compare the $\alpha = 1$ result to our $\alpha = 0.01$ simulation in fig. 4.1, we see that the dynamics are consistent—with the cloud falling, before splitting into sub-clusters.

The key difference is that the whole process occurs over a smaller vertical distance, for the same simulation time. This demonstrates that the resistivity of the medium, at this scale, only acts to decrease the speed of the falling cloud.

This effect is indicative of what we would expect to see if we increased the viscosity of our fluid. Hence, as viscosity is a measure of how resistive a fluid is to change, we can say that the medium has a holistic effect on the fluid, rather than affecting the particles on a local level.

If we now examine the result for the $\alpha = 5$ simulation, we begin to see a change in the general behaviour. We now have $L^2 > K$, which implies that the characteristic length scale of the fluid flow is greater than the permeability scale of the medium, as explained by Durlofsky and Brady in [13].

Rather than remaining compact as it falls, as with our previous simulations, we quickly see the cloud begin to stretch vertically. As the main cloud loses mass, we begin to see a diffusive effect, with the particles spreading out.

By the end of the simulation, the particles have dispersed much more, and fallen much less, than the previous simulations. We no longer see the torus formation and subsequent splitting phenomena, which occurred in the low- α Brinkman flow and Stokes flow simulations.

Due to the decreased permeability scale of the medium—relative to the length scale of the fluid—we are beginning to see the particles affected by the resistance on an individual level. The medium no longer has the porosity for the cloud to fall freely, causing the diffusive effect we see.

In the final simulation, for $\alpha = 10$, this diffusive effect is even clearer. The cloud falls very slowly and immediately begins to disperse. The concentration of particles becomes increasingly sparse, as the original structure of the cloud is quickly lost.

Previously, particles which escaped from the main cloud were left behind in the trailing vertical tail. Here, particles which escape are actually travelling further. By the end, the particles which have travelled the furthest have only fallen 5% as far as those in the $\alpha = 0.01$ simulation; the main bulk remains even higher.

These results should be physically intuitive—the decreased porosity means that larger clusters of particles will struggle to fall through the medium. Once a particle escapes the main group, it will experience less resistance and can hence travel further.

As discussed in section 3.2, large values of α in the Brinkman equations imply that the velocity is predominantly balanced by the pressure gradient and external forces. This results in a quasi-static flow, as discussed by Almi in [2], where the particles slowly move from areas of high pressure, to areas of low pressure.

As our particles are unrestricted in all directions, this pressure-driven flow causes the diffusive effect that we see. Particles leave the main cloud in all directions, moving towards the less densely packed—and therefore lower pressure—regions of the fluid. The external force of gravity then ensures that each particle maintains a negative vertical velocity component.

4.4 Analysing particle spread II

Many applications of Brinkman flows, such as the hydrodynamic modelling of groundwater flows, as discussed by Das in [11], have an intrinsic interest in particle dispersion. In section 2.5, we introduced a methodology for analysing the spread of particles—which we now return to.

We have seen that adjusting the characteristic permeability parameter, α , of our medium can result in two qualitatively different groups of outcomes. In low- α mediums, we saw similar behaviour to that observed in our Stokes simulations, with larger values of α decreasing the holistic speed of the fluid. For simulations where $\alpha > 1$, we began to see behaviour akin to Darcy's law, with a pressure-driven diffusive effect. Hence, we expect to see a significant difference in the average particle spread, as α increases.

We fix $N_0 = 2\,000$, to ensure comparable results, and split the simulations into two groups: $\alpha \leq 1$ and $\alpha > 1$. In fig. 4.3 and fig. 4.4, we see the local linear regression estimates of the average particle spread, for both groups of simulations.

Particle spread in low α Brinkman simulations

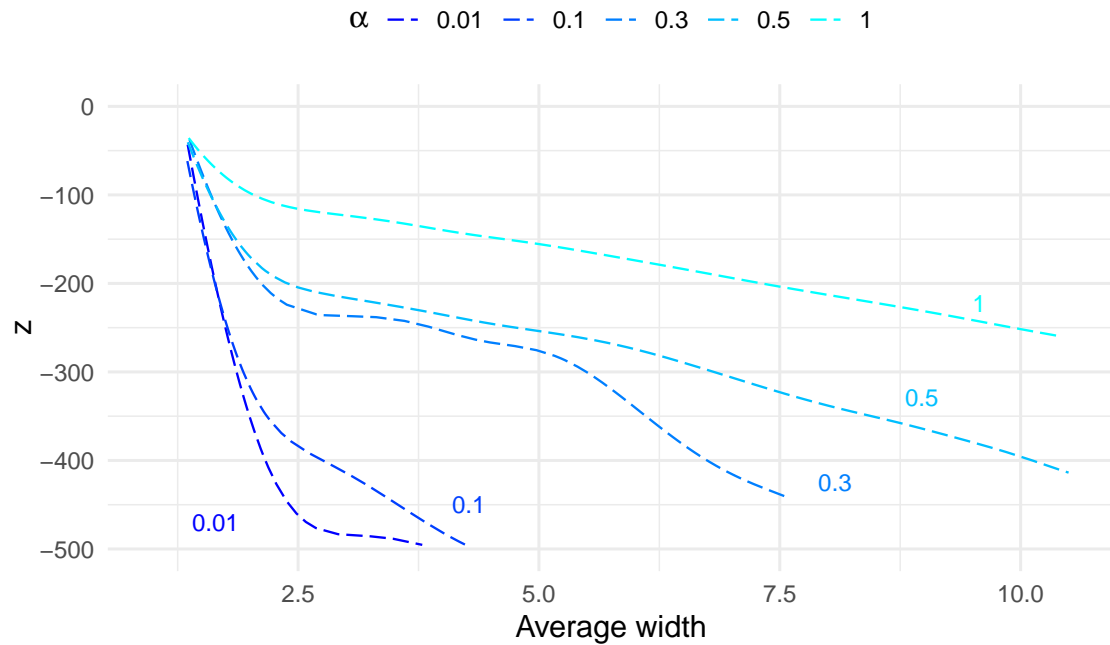


Figure 4.3: Local linear regression estimates of particle spread during Brinkman simulations, for $N_0 = 2000$ and $\alpha \in \{0.01, 0.1, 0.3, 0.5, 1\}$.

Particle spread in high α Brinkman simulations

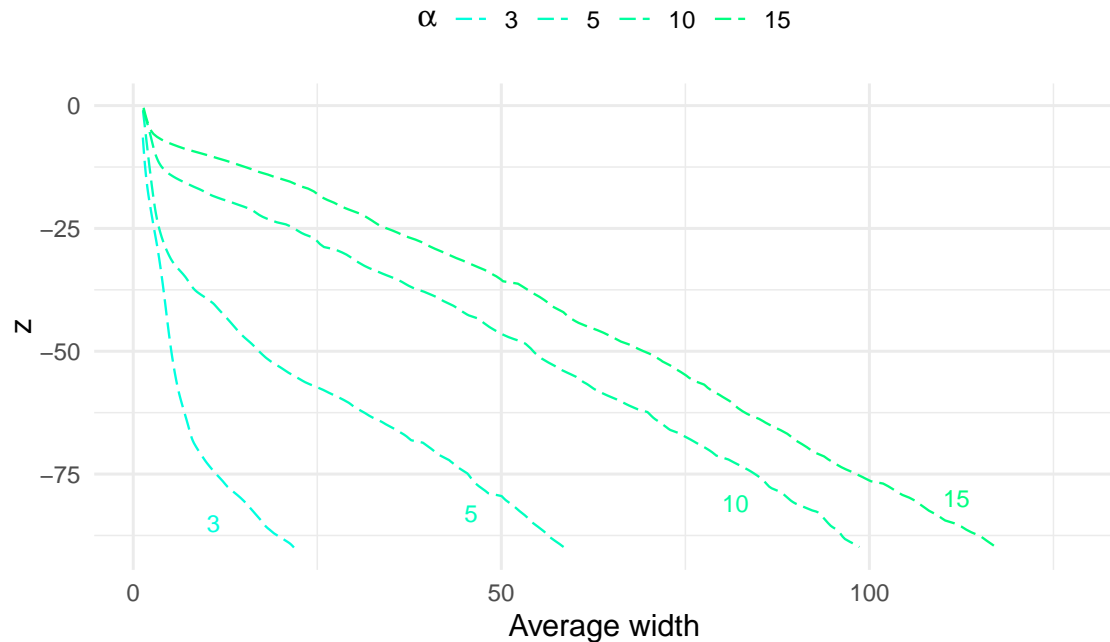


Figure 4.4: Local linear regression estimates of particle spread during Brinkman simulations, for $N_0 = 2000$ and $\alpha \in \{3, 5, 10, 15\}$

The results in fig. 4.3 align with our conclusions from fig. 2.9 and section 4.3. We see the widths gradually increase, until a splitting event occurs and the average particle spread jumps up—corresponding to the separation of the sub-clusters. As α rises, this splitting event occurs at a greater dimensionless height, due to the reduced speed of the clouds.

In fig. 4.4, we see the consequences of the diffusive effect displayed in fig. 4.2. It is important to note that the scale of the x -axis is a lot larger—and the scale of the z -axis a lot smaller—than in fig. 4.3, due to the general changes in dynamics.

As α increases, we see the average widths rise substantially. In each simulation, there is a section in which the width increases slowly, before a change occurs and it begins to grow quickly. The height at which this transition occurs corresponds to the distance the main particle cloud is able to travel, before completely dispersing. As we may expect, this height increases for larger values of α , as it becomes more difficult for the cloud to maintain structure as it falls.

The increasing width below this point is representative of the particles which have escaped the main cloud. As in fig. 4.2, the particles which escape diffuse quickly away from the main cluster, due to the pressure-driven flow. As this occurs in all directions, we see a rapid growth in particle spread. This diffusion occurs from a greater height as α rises, resulting in an increase to the final particle spread.

Overall, it is clear that the introduction of a porous medium has had a substantial impact on the particle spread. When α was low, the dynamics were consistent with the Stokes flow observations by Machu et al. in [24], and Metzger, Nicolas and Guazzelli in [25]. This resulted in particle dispersion which was highly comparable to our results in section 2.5.

For larger values of α , the decreased permeability scale of the medium, with respect to the length scale of the fluid, meant that the cloud could no longer freely evolve. This resulted in a pressure-driven diffusive effect, which led to a drastic increase in the average particle spread.

Chapter 5

Further model complexities

In this chapter, we implement a number of novel adaptations to the traditional point-particle simulation model. The simplicity of this model restricts its applicability to many physical systems—so we generalise our computational approach, in order to facilitate more complex analyses.

In [28], Singh, Seth and Hussain analysed the Brinkman flow of a nanofluid between two electrically conductive walls. These walls instigated a magnetic field across the fluid, which affected the behaviour of the flow. In [10], Daddi-Moussa-Ider and Vilfan extended the point-force model to a multitude of different geometries, successfully modelling a number of biological phenomena, such as cytoplasmic flow in cells.

Both of these examples illustrate the value of Brinkman flows, when additional complexities are introduced to the model.

5.1 Magnetised particle flow

Inspired by the works of Hatzikonstantinou and Vafeas in [20] and Singh, Seth and Hussain in [28], we first create a unique conceptual model of hydromagnetic flow, in a Brinkman regime.

In order to instigate a magnetic field in our model, we consider each point-particle to have some small, identical electric charge, q . Each charged particle will thus generate a small magnetic field.

The magnetic field \mathbf{B} at some point \mathbf{r}_1 , which arises from a moving point-charge currently positioned at \mathbf{r}_2 , is given by

$$\mathbf{B}(\mathbf{r}_1) \propto q \left(\frac{\mathbf{u}_2 \times \hat{\mathbf{r}}_{21}}{r_{21}^2} \right), \quad (5.1.1)$$

where \mathbf{u}_2 is the velocity of the moving charge, $\mathbf{r}_{21} = \mathbf{r}_2 - \mathbf{r}_1$, and $r_{21} = |\mathbf{r}_{21}|$ [18]. The proportionality constant depends upon the magnetic permeability of the medium. We avoid the need to specify this quantity by later absorbing all constants, including q , into a magnetic field parameter, which we will denote β .

The importance of this relation is that the magnetic field at some point \mathbf{r}_1 , emanating from a point-charge, acts perpendicular to both the velocity of the charge and the unit vector

pointing from \mathbf{r}_1 towards the charge. The strength of this field then decays proportionally to the squared distance between the point in the field, and the charge.

We note that the relation in eq. (5.1.1) holds when particle velocity is constant. As we are applying this to low Reynolds number fluids, we can assume this condition is approximately valid.

Furthermore, the relation in eq. (5.1.1) is derived from Maxwell's equations, which are linear [18]. As such, we can once again use the principle of superposition to combine the arising electromagnetic fields. We assume there are N_0 point-charges in our fluid—hence, we state that the net magnetic field at some particle i is given by

$$\mathbf{B}(\mathbf{r}_i) \propto \sum_{i \neq j}^{N_0} \left(\frac{\mathbf{u}_j \times \hat{\mathbf{r}}_{ji}}{r_{ji}^2} \right). \quad (5.1.2)$$

For a charged particle in a magnetic field, the force which acts upon the particle is given by the well-known Lorentz force

$$\mathbf{F}(\mathbf{r}) = q(\mathbf{u} \times \mathbf{B}),$$

where \mathbf{r} and \mathbf{u} are the respective position and velocity of the charged particle. Once again, the importance of this relation is that the force acts perpendicular to both the velocity of the particle, and the direction of the magnetic field.

Using eq. (5.1.2) to determine the net magnetic field at some particle i , we can subsequently state that the force which acts upon the particle—as a result of the magnetic contributions of the other particles—is given by

$$\begin{aligned} \mathbf{F}(\mathbf{r}_i) &\propto \mathbf{u}_i \times \sum_{i \neq j}^{N_0} \left(\frac{\mathbf{u}_j \times \hat{\mathbf{r}}_{ji}}{r_{ji}^2} \right), \\ &= \frac{\beta}{N_0} \mathbf{u}_i \times \sum_{i \neq j}^{N_0} \left(\frac{\mathbf{u}_j \times \hat{\mathbf{r}}_{ji}}{r_{ji}^2} \right), \end{aligned} \quad (5.1.3)$$

where β is our aforementioned magnetic field parameter. Note that we divide by N_0 , to standardise the scale of the force across simulations.

With this force relation, we return to our point-particle Brinkman model. As well as gravity, we now consider the arising electromagnetic force that acts on each particle. We intend to evaluate whether this simplified inclusion of magnetic forces has a significant effect on the evolution and dispersion of the particle cloud. Once again, we use the fundamental Brinkman regime for comparability and simplicity.

Recall that the velocity at particle i in our fundamental Brinkman regime (4.1.1) is given by

$$\mathbf{u}(\mathbf{r}_i) = \sum_{i \neq j} (\mathbf{F} H_1(r_{ij}) + (\mathbf{F} \cdot \mathbf{r}_{ij}) \mathbf{r}_{ij} H_2(r_{ij})). \quad (5.1.4)$$

In section 4.1, we assumed a constant gravitational force of $\mathbf{F}_g = (0, 0, -1)$. This gave us a simplified mobility matrix for the system of ordinary differential equations, in eq. (4.1.2). Explicitly, the only values which were calculated at each time-step were the respective displacements between each pair of particles, and the corresponding outputs of $H_1(r_{ij})$ and $H_2(r_{ij})$.

However, in order to implement our magnetic field set-up, we note that the external force acting on each particle is different, and variant at each time step. This provides a new level of complexity to our simulation.

We can express eq. (5.1.4) in the form

$$\mathbf{u} = \mathbf{MF}, \quad (5.1.5)$$

where \mathbf{u} and \mathbf{F} are vectors of length $3N_0$, and \mathbf{M} is a $3N_0 \times 3N_0$ mobility matrix. The vectors represent the three components of the velocity and force at a fixed time, for each particle. That is, $[\mathbf{u}]_{3(i-1)+j}$, for $j \in \{1, 2, 3\}$, represents the velocity components of particle i , for $i \in \{1 \dots N_0\}$, with the same logic applied to \mathbf{F} .

To understand the form of the mobility matrix, we first consider the specific interaction between two arbitrary particles, m and n . From eq. (5.1.4), the interaction between these particles is dependent upon \mathbf{r}_{mn} and the corresponding values of $H_1(r_{mn})$ and $H_2(r_{mn})$. Specifically, we can define the 3×3 sub-matrix, denoting the interaction between particles m and n , as

$$\mathbf{S}^{(m,n)} = H_1(r_{mn}) + (\mathbf{r}_{mn} \otimes \mathbf{r}_{mn})H_2(r_{mn}).$$

Alternatively, using Einstein notation, one could express this component-wise as

$$[\mathbf{S}^{(m,n)}]_{ij} = H_1(r_{mn})\delta_{ij} + [\mathbf{r}_{mn}]_i [\mathbf{r}_{mn}]_j H_2(r_{mn}).$$

The mobility matrix, \mathbf{M} , can then be considered an $N_0 \times N_0$ arrangement of these sub-matrices, for each pair of particles. Explicitly, we can express it as

$$\mathbf{M} = \begin{pmatrix} \mathbf{S}^{(1,1)} & \mathbf{S}^{(1,2)} & \dots & \mathbf{S}^{(1,N_0)} \\ \mathbf{S}^{(2,1)} & \mathbf{S}^{(2,2)} & \dots & \mathbf{S}^{(2,N_0)} \\ \vdots & \vdots & \ddots & \vdots \\ \mathbf{S}^{(N_0,1)} & \mathbf{S}^{(N_0,2)} & \dots & \mathbf{S}^{(N_0,N_0)} \end{pmatrix}. \quad (5.1.6)$$

We observe that, as $\mathbf{r}_{mn} = -\mathbf{r}_{nm}$, and $r_{mn} = r_{nm}$, it holds that $\mathbf{S}^{(m,n)} = \mathbf{S}^{(n,m)}$, which therefore implies that \mathbf{M} is symmetric. Furthermore, as $r_{ii} = 0$, we set the sub-matrices along the leading diagonal to a 3×3 zero-matrix, in order to avoid errors.

With this definition, eq. (5.1.5) can be written explicitly as

$$\begin{pmatrix} u_x(\mathbf{r}_1) \\ u_y(\mathbf{r}_1) \\ \vdots \\ u_z(\mathbf{r}_{N_0}) \end{pmatrix} = \begin{pmatrix} \mathbf{o} & \mathbf{S}^{(1,2)} & \dots & \mathbf{S}^{(1,N_0)} \\ \mathbf{S}^{(1,2)} & \mathbf{o} & \dots & \mathbf{S}^{(2,N_0)} \\ \vdots & \vdots & \ddots & \vdots \\ \mathbf{S}^{(1,N_0)} & \mathbf{S}^{(2,N_0)} & \dots & \mathbf{o} \end{pmatrix} \begin{pmatrix} F_x(\mathbf{r}_1) \\ F_y(\mathbf{r}_1) \\ \vdots \\ F_z(\mathbf{r}_{N_0}) \end{pmatrix}. \quad (5.1.7)$$

In order to simulate the system in eq. (5.1.7), we first need to evaluate the force vector, \mathbf{F} . To do this, we create a new function which, given all the current particle positions and velocities, calculates the Lorentz force acting on each particle, as in eq. (5.1.3).

Due to our standardisation of these forces, the magnitude of the resultant force at each point remains—on average—below one, for all considered values of β . This is important, as we then add the fixed gravitational force $\mathbf{F}_g = (0, 0, -1)$ to each particle. The largest component of the force therefore remains the negative z -component, ensuring we maintain the falling cloud premise.

At each time-step, we implement the `einsum` function from the NumPy package, in order to efficiently compute the right-hand side of eq. (5.1.7). Noting that our calculation of \mathbf{F} depends on the current particle velocities, as well as the positions, we also define a new global variable to track velocities. Set initially to be an array of zeroes, we incorporate a global update of this variable into our derivative function, which subsequently executes after every time-step of the solver. Thus, at each step, we first determine the value of \mathbf{F} , using the current particle positions and velocities, before using this to compute \mathbf{MF} .

By increasing the value of β , we are increasing the respective weighting of the Lorentz force, with respect to the gravitational force. This variable has no physical meaning in isolation, but we use it for simplicity to encompass the unknown magnetic properties in our medium, as previously described.

As our goal is to analyse how a magnetic field can affect particle spread, we take a characteristic permeability parameter of $\alpha = 5$. This ensures we instigate the pressure-driven diffusive behaviour, seen in section 4.3.

Furthermore, due to the increased computational complexity, we simulate a smaller number of particles, with $N_0 = 500$. The diffusive behaviour is less sensitive to the value of N_0 —compared to the low- α simulations—so this still ensures our results are comparable.

With these parameters established, we simulate the system given by eq. (5.1.7), for increasing values of β . Holistic overviews of the results can be seen in fig. 5.1, where we note that the axes have been limited for visual clarity.

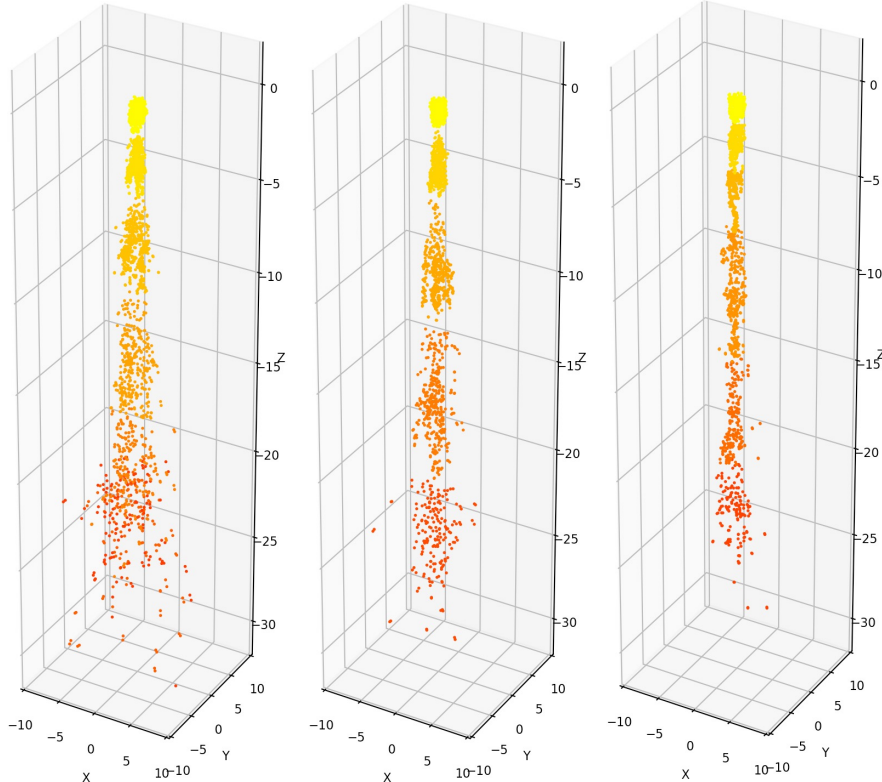


Figure 5.1: Comparative holistic overviews of the falling clouds in different magnetised Brinkman regimes, with $N_0 = 500$, $\alpha = 5$ and $\beta = 0.01, 1, 5$ (left to right).

The first graph acts as a reference point, as we take $\beta = 0.01$. With a value this small, the fluctuations in the particle forces which arise from the magnetic fields are negligible and the behaviour is thus comparable to a regular Brinkman simulation, as in section 4.3. We see the pressure-driven diffusive effect, as expected, implying our new method of computation is valid.

As we then increase the strength of the electromagnetic forces, taking $\beta = 1, 5$ in the latter two plots, we begin to notice a subtle change arise. We observe that the diffusive effect becomes increasingly nullified. The main cluster of particles maintains its structure for longer and fewer particles escape. This suggests that the magnetic fields are having a tangible effect—we are seeing an increase in the attraction between particles, reducing the rate at which the cloud disperses.

To evaluate the extent of this effect with greater scrutiny, we evaluate the system for more values of β , with a longer simulation time. In, fig. 5.2, we once again implement our dispersion analysis methodology, in order to visualise the resulting particle spread.

Particle spread in magentic field simulations for $\alpha = 5$

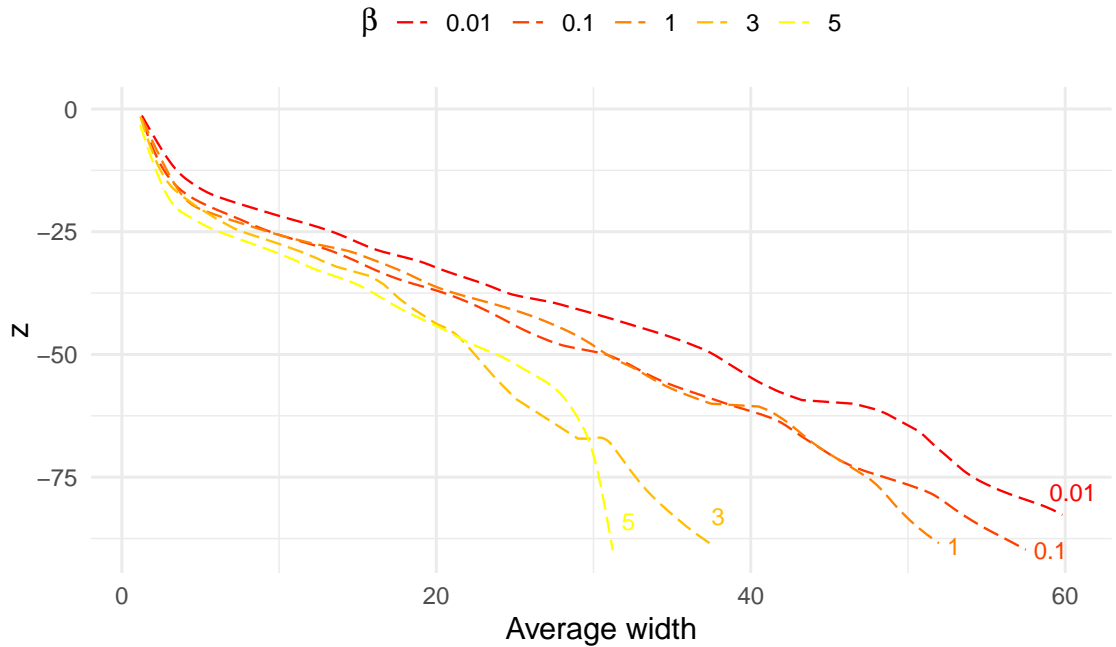


Figure 5.2: Local linear regression estimates of particle spread during magnetised Brinkman simulations, with $N_0 = 500$, $\alpha = 5$ and $\beta \in \{0.01, 0.1, 1, 3, 5\}$.

As the particle clouds fall further, the impact of the magnetic fields becomes more pronounced. At a vertical height of $z = -90$, the cloud in the $\beta = 5$ simulation has dispersed approximately half as much as the cloud in the $\beta = 0.01$ simulation.

The final average widths in the high- β simulations are still greater than those in the low- α Brinkman simulations we saw in fig. 4.3. However, it is clear that the implementation of magnetic interactions has gone some way to counteract the diffusive effects of the low-permeability medium.

The benefits of these analyses are twofold:

1. We have established that the presence of electromagnetic forces in a Brinkman regime can reduce the rate of particle dispersion. Due to the scientific relevance of hydromagnetic Brinkman flows, this has significant practical value.
2. During this process, we developed a more advanced computational framework, which allows us to simulate systems using any particle forces.

The second benefit is relevant in the context of potential future research. The direct applications of our magnetised simulations are somewhat limited, due to the lack of physical parameters and scientific context. However, more advanced models—where the precise forms of particle forces are known—could easily be modelled using this numerical framework, by simply adapting the force function as needed. This could extend our analysis to a number of fields where Brinkman flows are employed, from the modelling of water through coffee granules, to the transportation of metal ions in aqueous solutions.

5.2 An alternative particle geometry

As Machu et al. and Daddi-Moussa-Ider and Vilfan showed in [24] and [10] respectively, the initial configuration of particles in the point-force model has a significant effect on the subsequent behaviour. As such, we will extend our simulations beyond the context of a spherical cloud.

Furthermore, we will further illustrate the flexibility of the numerical framework established in section 5.1, by implementing additional inter-particle forces.

For this model, we assume that certain pairs of particles are attached by elastic springs, with fixed spring constant K . For two particles, positioned initially at \mathbf{r}_i and \mathbf{r}_j , attached by a spring, we denote their initial separation—corresponding to the resting spring length—as L . When these particles separate, we denote the change in distance—corresponding to the magnitude of the spring extension—as x . We visualise this spring set-up in fig. 5.3.

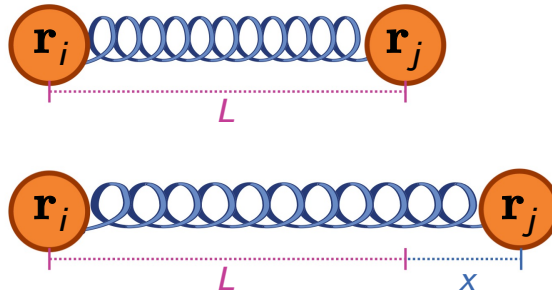


Figure 5.3: Visualisation of particle pair attached by a spring. The spring has rest length L and extension distance x .

We can then determine the explicit displacement of the spring, by $\mathbf{x} = \mathbf{x} \cdot \hat{\mathbf{r}}_{ij}$. Finally, we can deduce the force which is exerted by the spring, on the particle at \mathbf{r}_i , using the well-known Hooke's law, given by

$$\mathbf{F}(\mathbf{r}_i) = -K\mathbf{x}. \quad (5.2.1)$$

The corresponding force at \mathbf{r}_j is given by $\mathbf{F}(\mathbf{r}_j) = -\mathbf{F}(\mathbf{r}_i)$, by Newton's law of action and reaction.

With the spring-based framework established, we now establish the initial configuration of particles, and their respective spring connections. As previously noted, the aim of this section is to evaluate the influence of novel particle geometries, on simulation outcomes. As such, we choose to arrange the particles in the form of a 3D articulated body—using a careful placement of 32 regularised particles. We visualise this construction in fig. 5.4, noting that the black lines denote pairings of particles attached by a spring.

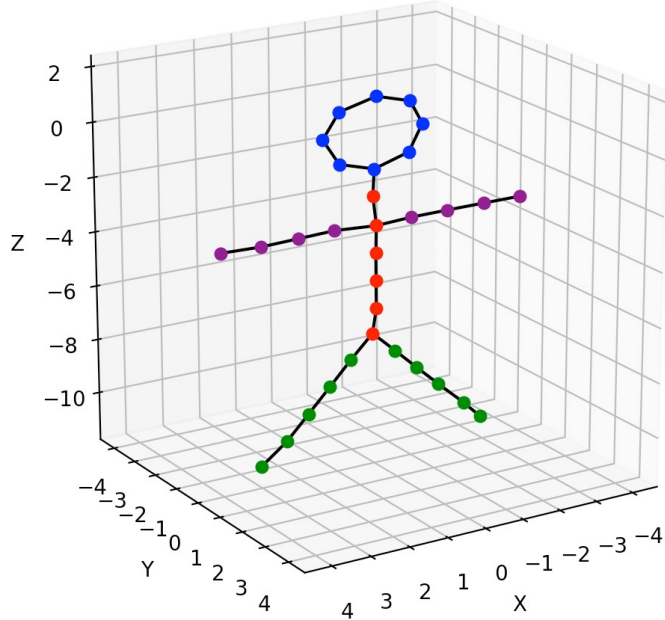


Figure 5.4: Initial 3D articulated body particle formation. Black lines denote the springs connecting particles.

We note that the particles are positioned such that all springs have initial rest length $L = 1$. However, we add some small, random perturbation to the y -coordinate of each particle, to ensure the articulated body does not lie entirely in the $y = 0$ plane.

In our previous simulations, we were interested in the general behaviour of our particle clouds, rather than the precise movement of individual particles. As such, we modelled each particle as a point-force, for computational simplicity and comparability. However, in this simulation, we model each particle as a regularised Brinkmanlet with width parameter $\delta = 0.01$, as in eq. (3.5.1). This ensures the local particle behaviour is as smooth as possible.

We simulate the system using the advanced computational framework we established in eq. (5.1.7). At each time-step, we first calculate the total spring force exerted on each particle, using eq. (5.2.1). Then, we add the gravitational force, $\mathbf{F}_g = (0, 0, -1)$, giving us the current value of \mathbf{F} .

Then, using the `einsum` function, we computationally approximate $\mathbf{u} = \mathbf{MF}$, where \mathbf{M} is the mobility matrix (5.1.6). Once again using the Runge–Kutta numerical method of order 5(4) to determine the time-steps, we iterate this process to simulate the articulated body falling through the Brinkman fluid.

In fig. 5.5, we see snapshots from the falling articulated body simulation, with $\alpha = K = 1$. This represents a Brinkman system which interpolates equally between the Stokes equations and Darcy's law. In addition, the relative strength of the springs connecting the pairs of particles is equal to the strength of the gravitational force, ensuring no force dominates the system.

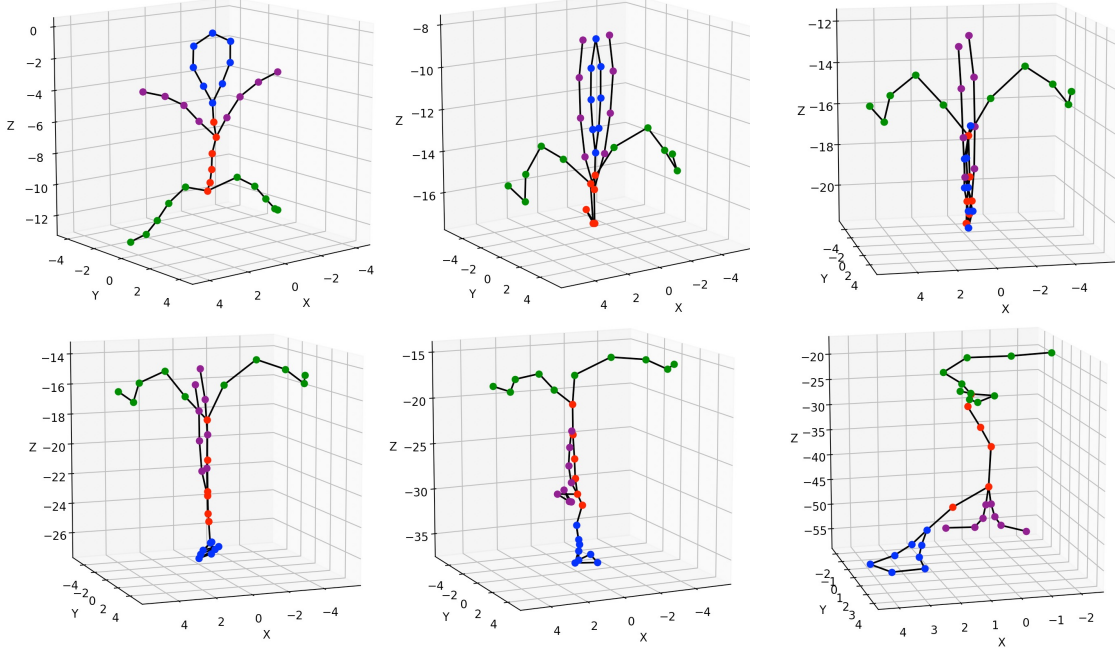


Figure 5.5: Falling articulated body simulation in an $\alpha = 1$ Brinkman regime. Black lines denote spring connections between particles, with spring constant $K = 1$. Particles are modelled as regularised forces, with width parameter $\delta = 0.01$.

We see the articulated body begins to fall, causing the limbs to elongate vertically. The spring forces from the torso then pull the head down, causing the body to invert. By the end of the simulation, the body has completely flipped around.

Due to the introduction of the spring forces, the particles all remain close together, and the body actually maintains its general structure as it falls—albeit, whilst undergoing an inversion. This demonstrates the tangible impact of the external forces, as the springs have prevented the particle dispersion which we would usually expect in a Brinkman system.

Whilst the examples in this chapter were mostly demonstrative, it is clear that the point-force model can be adapted to a vast array of physical contexts. Any arrangement of initial particle configurations and external forces could be modelled using our numerical framework—extending the application of this work to many scientific disciplines.

Chapter 6

Conclusion

Throughout this paper, we developed and explored a plethora of analytical and computational methods for solving low Reynolds number flows. We explored the effects of numerous model parameters and established a numerical framework, which allowed us to simulate an array of physical systems.

Beginning with the incompressible Navier–Stokes equations, we introduced the concept of the Reynolds number, allowing us to derive the Stokes equations. These equations model fluid flows in which the inertial forces completely dominate the viscous forces. Using Fourier transforms, we developed the general framework outlined by Lisicki in [22], to obtain the fundamental solution to the Stokes equations—the Stokeslet.

Due to the linearity of the Stokes equations, we were able to construct a foundation for numerical simulation by implementing a methodology proposed by Nitsche and Batchelor in [27]. We superposed Stokeslets, forming a cloud of point-particles. Using a modern implementation of Runge–Kutta integration, we then simulated this cloud as it sedimented under gravity, in a Stokesian fluid.

Implementing a range of initial conditions, we confirmed the previous findings of Nitsche and Batchelor [27], Machu et al. [24] and Metzger, Nicolas and Guazzelli [25]. For a smaller number of initial particles, the cloud maintained its structure, whilst particles were slowly lost in a trailing vertical tail. As the density of the cloud increased, this behaviour evolved into the formation of a torus. The cloud subsequently split into a number of sub-clusters in a descending cascade. Furthermore, we developed a framework for analysing the dispersion of particles in different simulations. We used a manual implementation of the local linear regression estimator, as presented by Fan in [15]. This allowed us to smoothly approximate the average particle spread, across a discretisation of vertical windows.

We then extended our consideration of low Reynolds number fluids to the context of flows through a porous medium. Such flows display qualitatively variant behaviour depending on the permeability of the medium. We thus introduced the Brinkman equations, which interpolates between viscous Stokes flows and the pressure-driven behaviour described by Darcy’s law.

To solve the Brinkman equations, we developed the general approach presented by Cortez et al. in [9]. After deriving the fundamental solution to the Brinkman equations—the Brinkmanlet—we then introduced a regularised force, through the use of blob functions. These functions provide a continuous approximation to the Dirac delta measure. Evaluating the system in the regularised regime then gave us flow solutions with smooth local behaviour at each particle.

Using these Brinkmanlets, we then returned to our particle cloud premise, and simulated the sedimentation through porous media. In the low- α limit, we confirmed the asymptotic alignment of the Brinkman equations with the Stokes equations. As the permeability of the medium then decreased, we observed the pressure-driven diffusive effect of the particles—as described by Darcy’s law. Using our framework for analysing particle dispersion, we observed that the spread of particles increased with α —with two distinct sets of dynamics, governed by the value of α .

In order to align our work with a greater number of physical systems, we then introduced a number of additional complexities to our model. We first developed a conceptual hydromagnetic flow model, by generalising our numerical framework. From this, we observed that the rate of particle dispersion could be restricted by electromagnetic forces within the fluid.

To illustrate the flexibility of our enhanced computational framework—as well as the importance of initial particle geometries—we developed a simplified model of a 3D articulated body. We modelled the body as a network of regularised Brinkmanlets, connected by elastic springs. We thus demonstrated the significance of external forces and particle configuration on the simulation results. More importantly, we demonstrated how easily our framework could be adapted to different practical models.

Throughout the simulations, we illustrated the individual impacts of each of the model developments. In fig. 6.1, we can see holistic simulation overviews from a Stokes flow simulation, a high- α Brinkman flow simulation, and a hydromagnetic Brinkman flow simulation.

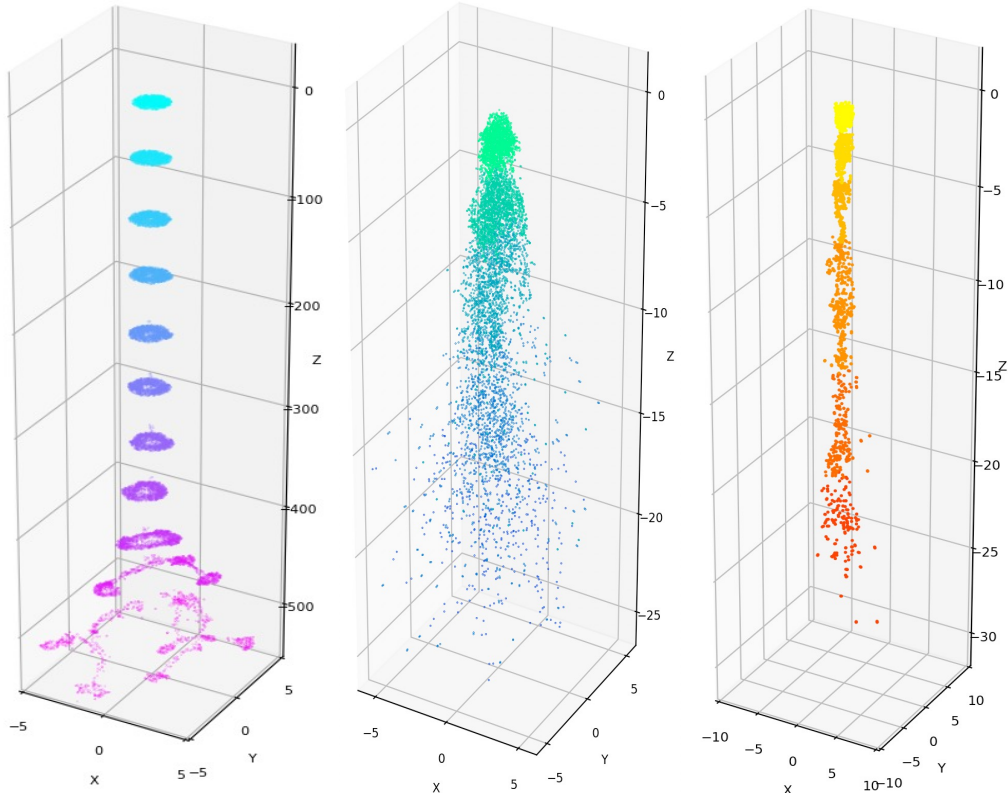


Figure 6.1: Holistic simulation overviews from Stokes flow, $\alpha = 10$ Brinkman flow and $\alpha = \beta = 5$ magnetised Brinkman flow (left to right).

By increasing α , we demonstrated the transition between Stokes flow dynamics, and the pressure-driven flow of Darcy's law. Then, by introducing electromagnetic forces between the particles, we were able to show the reduction in the rate of particle dispersion.

Looking ahead, there are a number of further developments which could be made to the models we have presented. The point-particle model has been shown to be highly informative, but it still lacks some physical accuracy. More advanced implementations, such as the neural network approach of Ma and Pan in [23], allow for the inclusion of complex interactive phenomena on a larger scale. Such approaches would reduce the uncertainty in the model, which could be of great value to a number of fields, such as the modelling of blood flow.

The applications of Stokes and Brinkman flows are plentiful. For any system where the particle forces and initial configuration are known, our computational framework could provide a reliable and efficient approximation of the behaviour. To improve the accuracy of these simulations further, we could consider the effects of different boundary conditions. In [7], Cortez describes how regularised forces are used to discretise complex boundaries, allowing for complete flow solutions to be obtained. Using our expressions for the regularised Brinkmanlets, we could apply this approach—alongside our advanced computational framework—to many models of scientific intrigue.

Bibliography

- [1] K Adachi, S Kiriyama and N Yoshioka. ‘The behavior of a swarm of particles moving in a viscous fluid’. In: *Chemical Engineering Science* 33.1 (1978), pp. 115–121.
- [2] Stefano Almi. ‘Quasi-static hydraulic crack growth driven by Darcy’s law’. In: *Advances in Calculus of Variations* 11.2 (2018), pp. 161–191.
- [3] George B Arfken, Hans J Weber and Frank E Harris. *Mathematical methods for physicists: a comprehensive guide*. Academic press, 2011, p. 463.
- [4] Abdon Atangana. *Fractional operators with constant and variable order with application to geo-hydrology*. Academic Press, 2017, pp. 19–21.
- [5] Thorsten Bosse et al. ‘Numerical simulation of finite Reynolds number suspension drops settling under gravity’. In: *Physics of Fluids* 17.3 (2005).
- [6] Hendrik C Brinkman. ‘A calculation of the viscous force exerted by a flowing fluid on a dense swarm of particles’. In: *Flow, Turbulence and Combustion* 1.1 (1949), pp. 27–34.
- [7] Ricardo Cortez. ‘The method of regularized Stokeslets’. In: *SIAM Journal on Scientific Computing* 23.4 (2001), pp. 1204–1225.
- [8] Ricardo Cortez, Lisa Fauci and Alexei Medovikov. ‘The method of regularized Stokeslets in three dimensions: analysis, validation, and application to helical swimming’. In: *Physics of Fluids* 17.3 (2005).
- [9] Ricardo Cortez et al. ‘Computation of three-dimensional Brinkman flows using regularized methods’. In: *Journal of Computational Physics* 229.20 (2010), pp. 7609–7624.
- [10] Abdallah Daddi-Moussa-Ider and Andrej Vilfan. ‘On force balance in Brinkman fluids under confinement’. In: *Journal of Fluid Mechanics* 1008 (2025), A11.
- [11] Diganta Bhushan Das. ‘Hydrodynamic modelling for groundwater flow through permeable reactive barriers’. In: *Hydrological processes* 16.17 (2002), pp. 3393–3418.
- [12] John R Dormand and Peter J Prince. ‘A family of embedded Runge-Kutta formulae’. In: *Journal of computational and applied mathematics* 6.1 (1980), pp. 19–26.
- [13] L Durlofsky and JF Brady. ‘Analysis of the Brinkman equation as a model for flow in porous media’. In: *Physics of Fluids* 30.11 (1987), p. 3329.

- [14] ML Ekiel-Jeżewska, B Metzger and E Guazzelli. ‘Spherical cloud of point particles falling in a viscous fluid’. In: *Physics of Fluids* 18.3 (2006).
- [15] Jianqing Fan. ‘Local linear regression smoothers and their minimax efficiencies’. In: *The annals of Statistics* (1993), pp. 196–216.
- [16] Giovanni P Galdi. *Navier-Stokes Equations: A Mathematical Analysis*. 2009.
- [17] Josephin Giacomini et al. ‘Water flow and transport in porous media for in-silico espresso coffee’. In: *International Journal of Multiphase Flow* 126 (2020), p. 103252.
- [18] David J Griffiths. *Introduction to Electrodynamics*. 1999.
- [19] Elisabeth Guazzelli and Jeffrey F Morris. *A physical introduction to suspension dynamics*. Vol. 45. Cambridge University Press, 2011.
- [20] PM Hatzikonstantinou and P Vafeas. ‘A general theoretical model for the magnetohydrodynamic flow of micropolar magnetic fluids. Application to Stokes flow’. In: *Mathematical Methods in the Applied Sciences* 33.2 (2010), pp. 233–248.
- [21] A Koponen, M Kataja and JJP Timonen. ‘Permeability and effective porosity of porous media’. In: *Physical Review E* 56.3 (1997), p. 3319.
- [22] Maciej Lisicki. ‘Four approaches to hydrodynamic Green’s functions—the Oseen tensors’. In: *arXiv preprint arXiv:1312.6231* (2013).
- [23] Zhan Ma and Wenxiao Pan. ‘Shape deformation, disintegration, and coalescence of suspension drops: Efficient simulation enabled by graph neural networks’. In: *International Journal of Multiphase Flow* 176 (2024), p. 104845.
- [24] Gunther Machu et al. ‘Coalescence, torus formation and breakup of sedimenting drops: experiments and computer simulations’. In: *Journal of Fluid Mechanics* 447 (2001), pp. 299–336.
- [25] Bloen Metzger, Maxime Nicolas and Élisabeth Guazzelli. ‘Falling clouds of particles in viscous fluids’. In: *Journal of Fluid Mechanics* 580 (2007), pp. 283–301.
- [26] MM Metzger and JC Klewicki. ‘A comparative study of near-wall turbulence in high and low Reynolds number boundary layers’. In: *Physics of Fluids* 13.3 (2001), pp. 692–701.
- [27] J. M. Nitsche and G. K. Batchelor. ‘Break-up of a falling drop containing dispersed particles’. In: *Journal of Fluid Mechanics* 340 (1997), pp. 161–175. DOI: [10.1017/S0022112097005223](https://doi.org/10.1017/S0022112097005223).
- [28] Jitendra Kumar Singh, Gauri Shanker Seth and Syed M Hussain. ‘Thermal performance of hydromagnetic nanofluid flow within an asymmetric channel with arbitrarily conductive walls filled with Darcy-Brinkman porous medium’. In: *Journal of Magnetism and Magnetic Materials* 582 (2023), p. 171034.
- [29] Christopher I Trombley and Maria L Ekiel-Jeżewska. ‘Basic concepts of Stokes flows’. In: *Flowing Matter* (2019), pp. 35–50.
- [30] Harry Wiffen. *HW-ProjectIV: Stokes and the Brinkmanlets*. Version 1.0.0. Apr. 2025. URL: <https://github.com/hwiffen/HW-ProjectIV>.
- [31] Z Zapryanov and S Tabakova. *Dynamics of bubbles, drops and rigid particles*. Vol. 50. Springer Science & Business Media, 2013.